

THE MAGELLANIC STREAM: BREAK UP AND ACCRETION ONTO THE HOT GALACTIC CORONA

THOR TEPPER-GARCÍA¹, JOSS BLAND-HAWTHORN¹, AND RALPH S. SUTHERLAND²

¹Sydney Institute for Astronomy, School of Physics, University of Sydney, NSW 2006, Australia and

²Research School of Astronomy and Astrophysics, Australian National University, Cotter Road, Weston, ACT 2611, Australia

Draft version 7th December 2024

Abstract

The Magellanic H I Stream ($\approx 2 \times 10^9 M_{\odot} [d/55 \text{ kpc}]^2$) encircling the Galaxy at a distance d is arguably the most important tracer of what happens to gas accreting onto a disk galaxy. Recent observations reveal that the Stream's mass is in fact dominated (3:1) by its ionized component. Here we revisit the origin of the mysterious H α (recombination) emission observed along much of its length that is overly bright ($\sim 150 - 200 \text{ mR}$) for the known Galactic UV background ($\approx 20 - 40 \text{ mR} [d/55 \text{ kpc}]^{-2}$). In an earlier model, we proposed that a slow shock cascade was operating along the Stream due to its interaction with the extended Galactic hot corona. But in view of updated parameters for the corona and mounting evidence that most of the Stream must lie far beyond the Magellanic Clouds ($d > 55 \text{ kpc}$), we revisit the shock cascade model in detail. While slow shocks are important in sustaining the observed levels of ionization, it now appears unlikely they can account for the bright H α emission if the corona is smooth. The H I gas is broken down by the shock cascade but mostly mixes with the hot corona without significant recombination. We conclude that the corona can be substantially mass-loaded with recent gas debris but this material is very difficult to observe directly.

Subject headings: galaxies: evolution – galaxies: interactions – hydrodynamics – instabilities – Magellanic Clouds – shock waves

1. INTRODUCTION

A unique opportunity to study the nature of neutral (accreted) gas in the (DM) halos of galaxies is provided by the circumgalactic environment of the Milky Way. Neutral gas is observed across half the sky in the form of high-velocity H I clouds (HVC; Oort 1970) at a Galactic latitude $|b| > 30^\circ$ with kinematic properties not consistent with the overall Galactic rotation (Wakker 2001). Among these, the clouds that make up the Magellanic Stream (MS) stand out in many respects.

Since its discovery (Wannier & Wrixon 1972; Mathewson et al. 1974), the precise origin of the MS and its formation mechanism have challenged our understanding of the Galaxy and the interaction with its satellites, the Small Magellanic Cloud (SMC) and the Large Magellanic Cloud (LMC). For several years, the MS was believed to be the product of either tidal (Fujimoto & Sofue 1976) or hydrodynamical (Meurer et al. 1985) interaction between the (halo of the) Milky Way and the LMC-SMC system, or a combination of these processes (Mastropietro et al. 2005).

Recently, accurate measurements of the proper motions of the LMC (Kallivayalil et al. 2006b) and the SMC (Kallivayalil et al. 2006a) indicate that these galaxies have been in a binary state for a time scale on the order of the Hubble time, and that the SMC-LMC system is probably in its first passage around the Milky Way (Besla et al. 2007). This 'first-infall' scenario of the SMC-LMC system into the potential well of the Milky Way implies that the gas along the MS moves on a highly eccentric orbit which spans a huge range of Galactocentric distances, from its source in the LMC-SMC system at roughly 55 kpc to 80 – 150 kpc above the South Galactic Pole (SGP) all the way to the tip of the tail (Besla et al. 2012, but see Jin & Lynden-Bell 2008).

Given its relative proximity, the Magellanic Stream has been extensively observed across the electromagnetic spectrum. Recombination optical emission (H α) along the MS was detected for the first time by Weiner & Williams (1996), and later confirmed by others (Reynolds et al. 1998; Putman et al. 2004;

Madsen 2012). Deep, all-sky radio surveys sensitive to the H I 21 cm transition such as the Leiden / Argentine / Bonn Galactic H I Survey (LAB; Kalberla et al. 2005) demonstrate the magnitude and the complexity of the MS. A shadowing experiment aimed at measuring the soft X-ray emission of the Galactic hot halo by comparing the emission on and off HVCs made the remarkable discovery that the emission is enhanced in the direction of the MS (Bregman et al. 2009). This result is important since it indicates that a strong interaction between the MS gas and the hot halo gas is taking place. Moreover, the data obtained by the recently completed Hubble Space Telescope (HST) Cosmic Origins Spectrograph (COS) UV absorption survey of the MS (Fox et al. 2013; Richter et al. 2013; Fox et al. 2014) now provides a wealth of information which is crucial to understand the mechanisms that determine the physical state of the gas.

Observations (Nidever et al. 2010) and radiative hydrodynamic models (Bland-Hawthorn et al. 2007) indicate that the MS is just breaking up, virtually providing a picture in real-time of gas disruption as a consequence of the interaction with the halo. The magnetic field as measured in the Leading Arm (LA; Putman et al. 1998) at the 'head' of the Stream appears to be coherent and strong enough to stabilize the gas against severe ablation and provide thermal insulation to inhibit total evaporation of the clouds (McClure-Griffiths et al. 2010). Nevertheless, the COS/HST UV observations of the MS by Fox et al. (2014) indicate that the warm ionized gas contributes at least *three times* as much mass as the neutral gas to a total mass on the order of $10^9 M_{\odot}$, thus suggesting that most of the gas that makes up the Stream will not survive as warm neutral gas. This observations lends support to the idea advanced by Bland-Hawthorn et al. (2007) that there is likely a vast reservoir of gas which is however invisible to us. The intriguing question is whether (and how much) of this material will ultimately become available for the Galaxy to continue to form stars.

Therefore, interpreting the observed properties of the Magel-

lanic Stream within the framework of a full radiative hydrodynamical model is a crucial step towards understanding the complex processes that eventually lead to the formation of discs in galaxies. Particularly challenging is the explanation of the mechanism behind the $H\alpha$ emission observed along the full extension of the Magellanic Stream. To date, there are arguably only two serious attempts to explain the Stream’s $H\alpha$ emission: A novel, theoretical model which invokes a powerful flare of UV radiation from the Galactic Centre (GC) as the main ionization mechanism of the Stream’s gas, powered by the accretion of material onto the central black hole (BH) of the Galaxy (Bland-Hawthorn et al. 2013); and a previous, radiative hydrodynamical model which claims that the optical emission can be produced by the ionization that results from a shock cascade along the Stream as a consequence of the interaction with the hot Galactic halo (Bland-Hawthorn et al. 2007). The GC flare model is inspired by two important circumstances: 1) The discovery of the γ -ray emitting bubbles observed by the *Fermi* satellite extending roughly 50° (10 kpc) from the GC (Su et al. 2010); 2) The observation that the brightest optical emission along the Stream is confined to a cone with half-angle $\theta_{1/2} \approx 25^\circ$ roughly centered on the SGP (Madsen 2012). In addition, this model has found support from the timescales and energy budget required to ionize the Stream, which are consistent with the results from jet-driven numerical models of the *Fermi* bubbles (Guo & Mathews 2012).

The shock cascade model, on the other hand, explains the observation that the brightest $H\alpha$ detections lie at the leading edges of the $H\text{ I}$ clouds that make up the MS (Weiner et al. 2002). However, this model may fail to produce the observed emission levels *if* the distance to the Stream at the SGP significantly exceeds $d \approx 55$ kpc, as suggested by recent dynamical models (Besla et al. 2012). The ‘failure’ of the shock cascade model is based on the implicit assumption that the density of the halo decreases strongly with Galactocentric distance as $\propto r^{-2}$. But it is possible that this assumption is false. Therefore, a revision of the latter model is due. This is the main motivation for the present paper. Note that throughout the paper we assume a flat, dark-energy- and matter (baryonic and cold dark-matter; CDM) dominated Universe, and a cosmology defined by the set of parameters (relevant to this work) $h = 0.7$, $\Omega_m = 0.3$, and $\Omega_\Lambda = 0.7$.

In a nutshell, the goal of this study is to investigate the strength of the recombination ($H\alpha$) emission produced by the interaction of the MS gas with the Galactic corona at a range of Galactocentric distances, exploring different coronal parameters, this is, adopting different density and temperatures profiles of the gas sitting at rest in a fixed dark-matter (DM) potential.

2. MODELING THE GALACTIC CORONA

The density and temperature structure of the Galactic corona is largely determined by the underlying gravitational potential. The potential, in turn, is determined by the three main components of the Galaxy: the stellar bulge, the stellar and gaseous disc, and the DM halo. Given the mass of the bulge ($2 \times 10^{10} M_\odot$; Portail et al. 2015) and the disc ($6 \times 10^{10} M_\odot$; Kafle et al. 2014), these components are expected to dominate the Galactic potential only at $r \lesssim 5$ kpc and at $r \lesssim 15$ kpc, respectively. In fact, the DM halo dominates the Galactic potential at all distances, with a similar contribution from the disc at scales comparable to its length (Appendix A). The distance to the nearest point of the MS is believed to be $d \approx 55$ kpc, which roughly corresponds to the average distance to the Large

Magellanic Cloud (LMC) $d \approx 50$ kpc (Walker 2012), and the distance to the Small Magellanic Cloud (SMC) $d \approx 60$ kpc (Graczyk et al. 2014). Consequently, in modeling the interaction of the Magellanic Stream with the Galactic corona, it is safe to ignore the contributions to the potential from the bulge and the disc, and to focus instead on the DM halo only.

2.1. The Galactic DM halo

We model the DM halo of the Galaxy assuming it is well described by a single-component isothermal sphere. As it turns out, this choice does not significantly affect our results, since the relevant properties of an isothermal DM halo are very similar to those assuming a other physically viable models (see below). We opt for such a model given its solid physical foundation, with properties that can be derived from first principles starting from a few basic assumptions: the system is spherically symmetric and self-gravitating; the particles (of mass m) composing the system are collisionless; their velocities obey a Maxwell-Boltzmann distribution; and the potential is stationary, which implies that the total energy is conserved.¹

The *scale-free* potential, W , and the *scale-free* density profile, y , of an isotropic isothermal sphere are defined by the following system of ordinary differential equations in terms of the scale-free coordinate x (King 1966):

$$\frac{1}{x^2} \frac{d}{dx} \left(x^2 \frac{dW}{dx} \right) = -9 y(x), \quad (1)$$

$$y(x) = \exp[W(x)]. \quad (2)$$

Appropriate boundary conditions are, for example, the requirement that both the potential and the force vanish at the origin, i.e. $W(0) \equiv 0$ and $W'(0) \equiv 0$, respectively, which implies $y(0) = 1$. Note that $W(x) \leq 0$ for $x \geq 0$. Even though this system of equations has no analytic solution, it can be integrated numerically to values $x \ll 1$ to (nearly) arbitrary precision.

The connection between the scale-free quantities and their physical counterparts is given by

$$r = r_c x; \quad \rho_{\text{iso}}(r) = \rho_c y(x); \quad \Phi(r) - \Phi_0 = \sigma^2 W(x) \quad (3)$$

where ρ_c , r_c , and σ are the central density, the core radius, and the velocity dispersion, respectively, and $\Phi_0 \equiv \Phi(r = 0)$ is the value of the physical potential at the origin. The velocity dispersion, which is uniform (constant) for an isothermal sphere, defines the temperature of the system of particles through the relation $T = (m/k) \sigma^2$, where k is Boltzmann’s constant.²

A solution corresponding to a particular physical system is obtained by fixing two of these three parameters (or any other two independent physical quantities of the system, for that matter); the third parameter is tied to the other two through the relation (King 1966)

$$\frac{r_c^2 \rho_c}{\sigma^2} = \frac{9}{4\pi G} \quad (4)$$

where G is Newton’s constant.

¹ More formally, a isothermal sphere is a system whose distribution function in phase space is a steady-state solution of the collisionless Boltzmann equation, and thus, given its symmetries in both space and time (isotropy, time-independence), it is a function of the total energy only (Jeans 1915’s theorem). Such a system is said to be *ergodic* and is the simplest non-trivial model of this type. More elaborated models are the so-called *truncated* isothermal sphere models (see Michie & Bodenheimer 1963; King 1966).

² See Mohr et al. (2012) for a high-precision value and corresponding uncertainty of this and other fundamental physical constants used throughout this paper.

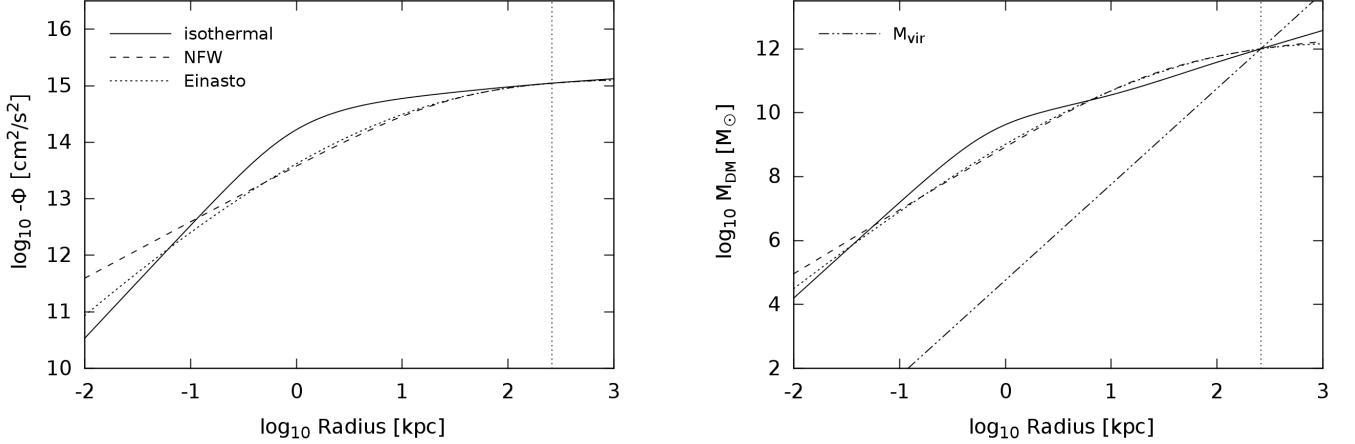


FIG. 1.— Potential (left) and enclosed mass (right) of the Galactic DM halo. The different curves correspond to different underlying density profiles, indicated by the legend in the left panel. The line of constant slope in the right panel shows the relation $M_{vir}(r)$ given by equation (7). Note that the potential and the mass of all profiles have been matched at the virial radius of the Galaxy, $r_{vir} \approx 260$ kpc, indicated by the vertical line in both panels. See also Table 1.

Given the underlying assumptions of the model, a single-component, isothermal sphere is a viable choice to describe a self-gravitating system of collisionless, DM particles, i.e. a DM halo (q.v. Sutherland & Bicknell 2007). Alternatives include the *Navarro-Frenk-White* (NFW) model, characterized by a radial density profile of the form (Navarro et al. 1996, and references therein)

$$\rho_{NFW}(r) = \frac{\delta_{th} \rho_{crit}}{(r/r_s)(1+r/r_s)^2}, \quad (5)$$

where δ_{th} defines a threshold density contrast with respect to the critical density of the Universe, ρ_{crit} , and r_s is a characteristic scale length; and the Einasto (1965) profile, which can be expressed as (Retana-Montenegro et al. 2012)

$$\rho_{EIN}(r) = \rho_s \exp \left\{ -\frac{2}{\alpha} \left[\left(\frac{r}{r_s} \right)^\alpha - 1 \right] \right\} \quad (6)$$

where ρ_s is a characteristic density and α is a free parameter. Numerical simulations of structure formation indicate that an Einasto profile with $\alpha \approx 0.18$ describes well the radial structure of DM halos (Gao et al. 2008).

Regardless of the model adopted, if the density profile $\rho(r)$ is known, a general formalism can be applied which allows to calculate scale-free quantities (i.e., mass, potential) and their corresponding scale parameters. The latter can be adjusted on a case-by-case basis to describe a particular physical system (see Appendix B).

In order to specify our isothermal DM halo, and to compare its properties to other commonly adopted models, we proceed as follows. We fix the virial mass M_{vir} and the concentration $x_{vir} \equiv r_{vir}/r_c$ of the NFW DM halo to $M_{vir} = 10^{12} M_\odot$, and $x_{vir} = 15$, respectively, which correspond to the values of the DM halo of the Galaxy as derived by Kafle et al. (2014, see their Figure 8). Note that fixing the virial mass implicitly fixes the virial radius and the circular velocity at the virial radius.³ Our adopted value for the virial mass implies

$$r_{vir} = \left(\frac{3 M_{vir}}{4\pi \Delta_c \rho_{crit}} \right)^{1/3}. \quad (7)$$

³ The virial mass and the virial radius are linked to one another through the relation

$r_{vir} \approx 260$ kpc and a value for the virial (circular) velocity $v_{vir} \equiv (GM_{vir}/r_{vir})^{1/2} \approx 130$ km s⁻¹, respectively. Then, we calculate the scale parameters for the isothermal and the Einasto DM halos by requiring that the virial mass and the *physical* potential at the virial radius in each case match the corresponding values of the NFW DM halo. Table 1 summarizes our assumed values and lists the derived values of the relevant scaling parameters for each of the halo models we consider: isothermal sphere (ISO); Einasto (EIN); and Navarro-Frenk-White (NFW). The values in bold font face indicate fixed (i.e. input) parameter values, while those in regular font face indicate derived parameter values. The differences worth mentioning are: the gas mass enclosed within r_{vir} for the Einasto profile, which is a roughly a factor two higher compared to the other models; the scale radius of the isothermal halo, which is significantly smaller compared to the other halo models; and the temperature (velocity) scale for the NFW profile, which is slightly higher with respect to the Einasto and isothermal profiles. Note that $T_{DM} < 10^6$ K in all models. Figure 1 shows the potential and mass of each of these DM halo models.

2.2. The density profile of a smooth Galactic corona

It has long been known that the potential well of the Galaxy is filled with a diffuse, hot, gaseous component (or corona; Spitzer 1956). However, the origin of this gas, its thermodynamic state, its physical properties, its extension and hence its total mass, are still unknown. A recent attempt to constraint the density structure and the total mass of the corona concluded that its total gas mass amounts to $\sim 10^{10} M_\odot$ within r_{vir} (Miller & Bregman 2013, 2015). This important result relies on the assumptions that the corona is smooth, in collisional ionization equilibrium, and isothermal, with a temperature of 2×10^6 K. While the gaseous halo of the Galaxy is most likely not smooth nor strictly isothermal (Yao & Wang 2007), the

Here, $\Delta_c \rho_{crit}$ is the average density within r_{vir} of a DM halo of mass M_{vir} (Gunn & Gott 1972). The overdensity Δ_c (with respect to the critical density) depends on redshift, z , and the cosmology through the matter-density parameter, Ω_m , and the dark-energy density parameter, Ω_Λ (Bryan & Norman 1998). Our adopted values for the cosmological parameters yield $\rho_{crit} \approx 9.20 \times 10^{-30}$ g cm⁻³ and $\Delta_c \approx 101$. Note that we define the virial radius at $z = 0$.

TABLE 1
DM HALO PROPERTIES

	Isothermal	Einasto	NFW
M_{vir} [$10^{12} M_{\odot}$]	1.00	1.00	1.00^a
r_{vir} [kpc]	259	259	259
v_{vir} [km s^{-1}]	129	129	129
x_{vir}	433	13.8	15.0^a
Φ_{vir} [$10^{15} \text{ cm}^2 \text{ s}^{-2}$]	-1.11	-1.11	-1.11
r_s [kpc] ^b	0.60	18.8	17.3
v_s [km s^{-1}] ^c	90.1	82.4	104
$M_{gas}(r_{vir})$ [$10^{10} M_{\odot}$] ^d	1.41	3.03	1.32
T_{DM} [10^5 K] ^e	5.81	4.85	7.73

NOTE. — Fixed parameter values are shown in bold face; derived values, in normal font face. See Appendix B for details. ^aFrom Kafle et al. (2014, their Figure 8). ^bCorresponds to the *scale* radius for the Einasto and NFW profiles, and to the *core* radius r_c for the isothermal sphere. ^cCorresponds to the *scale* velocity for the Einasto and NFW profiles, and to the *velocity dispersion* σ for the isothermal sphere. ^dObtained from equation (12), assuming $\tau \equiv 1$ and $\mu = 0.59$ (see Section 2.2). ^eTemperature assigned to the DM assuming $\tau \equiv 1$ (equation 9) and $a \equiv v_s$ (equation 8).

mean temperature of the gas inferred from its associated X-ray emission appear remarkably uniform across the sky (Henley et al. 2010).

Given this circumstance, we model the corona of the Galaxy as a smooth, spherically symmetric component consisting of an ideal gas at a constant temperature T_{gas} and in hydrostatic equilibrium with the DM potential of an isothermal sphere. It follows that the gas density ρ and the gas pressure P are linked by $P = \rho k T_{gas} / \mu m_u$. Here, m_u is the atomic mass unit, and $\mu \equiv \rho/n m_u$ is the mean molecular weight defined in terms of the mass density and the particle density n . The derivative of the pressure with respect to the density defines the isothermal sound speed,

$$a^2 = \frac{k T_{gas}}{\mu m_u}, \quad (8)$$

which is constant. Then, the condition of hydrostatic equilibrium ($\nabla P = -\rho \nabla \Phi$) with the DM potential Φ implies that the density profile of the corona is

$$n(r) = n_0 \exp \left[\frac{\Phi(r) - \Phi_0}{a^2} \right].$$

Note that the above equation is valid only if the self-gravity of the gas is negligible, which is justified in the case of the Galaxy given that the inferred gas mass of the hot halo is on the order of 10^{-2} the mass of the DM halo (Suto et al. 1998).

The virial temperature of the dark matter (halo) potential follows from equation (8) and the equivalence $a^2 \equiv \sigma^2$ (see Table 1),

$$T_{DM} \equiv \frac{\mu m_u}{k} \sigma^2. \quad (9)$$

It worth emphasising that the above is merely an *equivalent* temperature, as μm_u is not literally the DM particle mass (which is currently unknown).

It is then straightforward to show that the distribution of the gas in the potential is effectively determined by the *thermal ratio*⁴ (Cavaliere & Fusco-Femiano 1976)

$$\tau \equiv \frac{T_{DM}}{T_{gas}} = \sigma^2/a^2, \quad (10)$$

⁴ Note that the designation of thermal ratio by the Greek letter β is widespread in the literature, but we choose to adopt its original designation.

Indeed, using the relation between the physical potential Φ and the scale-free potential W (equation 3), together with the expression for τ , the density profile can be recast as

$$n(r) = n_0 \exp [\tau W(r/r_c)], \quad (11)$$

The total gas mass within r for a particular value of τ follows from the integral of n over the appropriate volume,

$$M(r) = 4\pi \mu m_u \int_0^r n(x) x^2 dx. \quad (12)$$

Since we are interested in distances $r \gtrsim 55$ kpc corresponding to the distance of the main body of the Magellanic Stream, it is relevant to analyze the asymptotic behavior of n for large values of r . In the regime where $r \gg r_c$, the potential of a true isothermal sphere behaves as $\Phi(r) \approx 2\sigma^2 \log r$. Consequently, the density of the gas behaves as

$$n(r) \propto r^{-2\tau}. \quad (13)$$

Clearly, the density field of gas in hydrostatic equilibrium with a fixed potential will be different for different gas temperatures. It follows that if the gaseous halo is ‘hotter’ than the DM particles (i.e. $\tau < 1$), then the density falls off more gently with radius. For instance, in the particular case of $\tau = 1/2$, the density behaves approximately as $n \propto r^{-1}$ at $r \gg r_c$. Conversely, large values of τ imply lower densities in the outer region of the halo, which in turn leads to weaker hydrodynamic interactions (at a fixed distance). Note that the definition of τ allows us to control the gas temperature by varying τ .

In the following we consider values of τ in the range [0.5, 1.5] only. We ignore values of $\tau < 0.5$, since these yield overly shallow density profiles, which are inconsistent with observations, as we show below. Note that values $\tau > 1$ imply that the gas has cooled *below* the (virial) temperature of the DM halo, and is more concentrated with respect to gas with $\tau < 1$. We choose the set of values $\tau \in \{1.5, 1.0, 0.75, 0.5\}$ as representative of this range. These, together with the value of the velocity dispersion of our isothermal DM halo model (Table 1) imply gas temperatures $T_{gas} \in \{0.39, 0.58, 0.77, 1.16\} \times 10^6$ K, respectively (Table 2). This range of gas temperatures is broadly consistent with estimates of the temperature of the Galactic hot halo (Snowden et al. 2000), albeit lower than the observed mean (but see Nuza et al. 2014).

Figure 2 displays the density profile (left panel) and the mass within r (right panel) given by equations (11) and (12), respectively, for our adopted values of τ in the relevant range $10 \text{ kpc} < r < r_{vir}$ (where the bulge and the disc are expected to contribute negligibly to the Galactic potential). For comparison, we include in this figure the density profile of the Galaxy inferred from observations (Miller & Bregman 2013, 2015), and the average density profile of a MW type galaxy predicted by a constrained simulation of galaxy formation (Nuza et al. 2014). Note that we have scaled our models and the result by Miller & Bregman (2013, 2015) to a fiducial value $n = 10^{-4} \text{ cm}^{-3}$ at 55 kpc, taking into account the difference in mean molecular weight due to difference in the adopted value of the halo metallicity ($Z = 0.1 Z_{\odot}$ rather than their $Z = 0.3 Z_{\odot}$; see Section 3).

As a consistency check, we compare the gas mass implied by each of our models to the upper limit on the Galactic gas mass within r_{vir} set by the mean baryon-to-total mass ratio $f_b \equiv \Omega_b/\Omega_m$ of the Universe. The most recent estimates of the

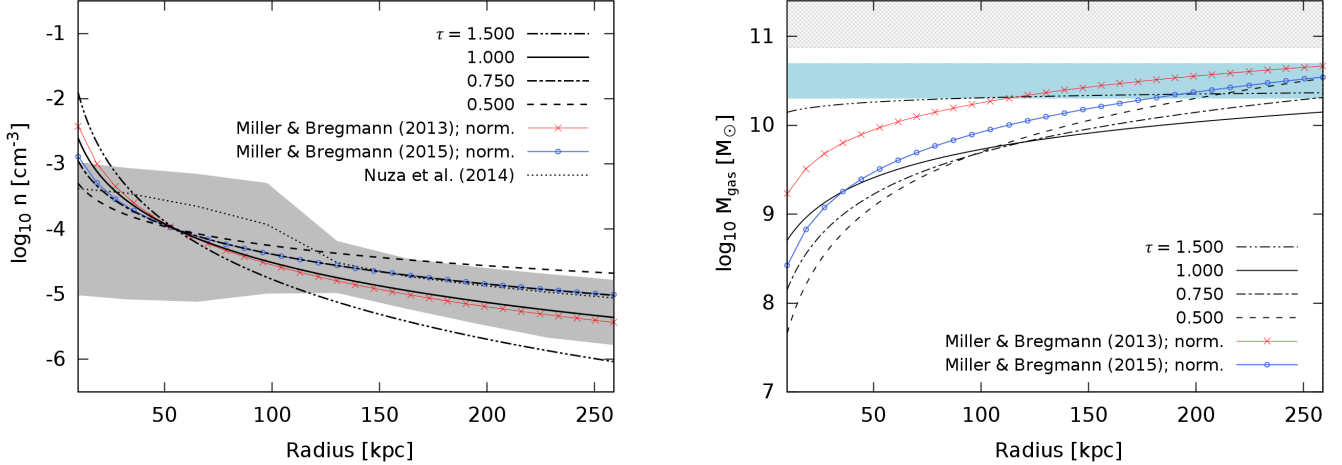


FIG. 2.— Left: Density profile (equation 11) for different values of τ . Also shown are the density profile of the Galaxy inferred from observations (Miller & Bregman 2013, 2015), and the average density profile of a MW type galaxy predicted by a constrained simulation of galaxy formation (Nuza et al. 2014); the grey shaded area reflects the scatter in the density along random directions of their simulated MW hot halo. Note that all the models (with exception of the Nuza et al. result) have been scaled to $n = 10^{-4} \text{ cm}^{-3}$ at 55 kpc. Right: Gas mass enclosed within a given radius (equation 12) for each of the density profiles shown in the left panel (except the Nuza et al. profile). The blue, horizontal band indicates the range of Galactic halo gas masses within $r \approx 250$ kpc inferred from observations (Miller & Bregman 2015). The grey hatched area on the top of the panel indicates the range of gas masses which are too large to be consistent with the (mean) cosmic baryon-to-total mass ratio $f_b \approx 0.16$ (see text for details).

TABLE 2
ISOTHERMAL GASEOUS HALO PROPERTIES

τ	T_{gas} [10^6 K]	$M_{gas}(r_{vir})$ [$10^{10} M_{\odot}$]	Density Factor ^a [10^{-2}]
0.5	1.16	3.36	1.91
0.75	0.77	2.06	26.4
1.0	0.58	1.41	365
1.5	0.39	2.33	6994

NOTE. — ^a Gives the factor by which the scale-free density y (for a given τ) needs to be rescaled to yield 10^{-4} cm^{-3} at $d = 55$ kpc.

baryon and cold dark matter mass densities $\Omega_b h^2 = 0.02205 \pm 0.00028$ and $\Omega_c h^2 = 0.1199 \pm 0.0027$ (Planck Collaboration 2014) imply $f_b \approx 0.16$. This value, together with the total mass of the Galaxy ($M_{tot} \sim 10^{12} M_{\odot}$) allow for a maximum gas mass of the Galaxy within r_{vir} below $10^{11} M_{\odot}$. As shown in Figure 2, all our models predict masses within r_{vir} below this limit, while still being consistent with the range of gas masses inferred from observations (with exception perhaps of the $\tau = 1$ model). Note that a density profile shallower (steeper) than the $\tau = 0.5$ (1.5) model would be largely inconsistent both with observations and simulations. Similarly, a value of n (at 55 kpc) significantly *higher* than our fiducial value would result in a gas mass inconsistent with this limit.

It is worth emphasising that the $\tau = 0.75$ model displays the best performance in terms of both the density profile and the gas mass enclosed within a given radius. Given that, in addition, our models reproduce by construction the relevant properties of the Galactic DM halo, we are confident that this model in particular provides a self-consistent and well founded description of the Galactic corona.

3. NUMERICAL EXPERIMENT

We simulate the passage of the Stream through the Galactic hot halo by means of a 3-dimensional (3D) ‘wind-tunnel experiment’, following Bland-Hawthorn et al. (2007). In brief, we place a warm and essentially neutral gas cloud at a distance r_{MS} initially at rest with respect to the computational volume,

and exposed it to a hot wind at a constant temperature T_h (for a fixed τ) and constant density n (for a fixed τ and r_{MS}) flowing with velocity \vec{v}_h under a fixed ‘angle of attack’ ϑ with respect to the gas cloud (see below). The warm gas is assumed to be initially in a state of pseudo-equilibrium with the hot gas (see equation 14). The relevant parameters of the simulation are thus: the density structure and the initial temperature of the warm neutral gas; the density and temperature of the hot gas; the metallicity of each component; the mean cloud-to-halo density ratio (or overdensity) $\eta \equiv \rho_w/\rho_h$; and the mean cloud-to-halo pressure ratio $\xi \equiv P_w/P_h$.

3.1. Code

We choose the high-resolution, multi-phase, shock-capturing hydrodynamic grid-based code FYRIS ALPHA (Sutherland 2010), especially developed for astrophysical applications. The code solves the fluid dynamic equations in one, two, and three dimensions as required. It has been shown to be fast, robust and accurate when compared to similar codes, and it performs well when subject to a standard suite of test cases as developed by Liska & Wendroff (2003). A unique feature of the FYRIS ALPHA code is that it includes non-equilibrium cooling through time-dependent ionization calculations. In addition, the code allows for the use of a variable equation of state (EoS) through a variable adiabatic index γ and / or a variable mean molecular weight μ . These aspects are of particular importance due to the expected difference in the relevant time-scales which determine the physical state of multi-phase gas.

3.2. Observational constraints, initial conditions, and set-up

The proper motion of the Large Magellanic Cloud (LMC) has recently been measured using *HST* data, yielding an orbital velocity $v_{LMC} = 378 \pm 18 \text{ km s}^{-1}$ (Kallivayalil et al. 2006b). Based on this result, we set the speed of the hot wind to $v_h = 350 \text{ km s}^{-1}$. Also, we adopt a value for the angle of attack $\vartheta = 24^\circ$, such that the (shear) velocity of the hot wind is given by $\vec{v}_h = (v_h \cos \vartheta, v_h \sin \vartheta, 0) = (320, 141, 0) \text{ km s}^{-1}$. Note that our results are fairly insensitive to the adopted value of ϑ , as long as $\vartheta \gg 0$ and $\vartheta \ll \pi/2$, which is supported by the

believe that the orbit of the Magellanic Stream is likely neither radial nor tangential with respect to the gaseous Galactic halo.

The Stream’s mean metallicity away from the MC is now well constrained to $Z \approx 0.1 Z_{\odot}$ (Richter et al. 2013; Fox et al. 2014). In contrast, the metallicity of the halo gas is still uncertain, although pulsar dispersion measures towards the LMC suggest $Z \gtrsim 0.3 Z_{\odot}$ (Miller & Bregman 2015). We opt for a conservative⁵ value for the metallicity of the halo of $Z = 0.1 Z_{\odot}$. We adopt a hydrogen, helium, and heavy-element mass fractions $X = 0.715$ and $Y = 0.270$, respectively (solar bulk composition; Asplund et al. 2009).

TABLE 3
RELEVANT SIMULATION PARAMETERS / INITIAL CONDITIONS

Parameter	Value	Remarks
T_h [K]	10^6	Halo gas temperature (approximate) ^a
T_w [K]	10^3	Initial cold gas temperature (approximate) ^b
η	100	Initial ratio of cloud to halo density
ξ	0.1	Initial ratio of cloud to halo pressure
$Z_h [Z_{\odot}]$	0.1	Halo gas metallicity
$Z_w [Z_{\odot}]$	0.1	Stream’s metallicity
n [cm^{-3}]	10^{-4}	Total particle density at 55 kpc
θ [$^{\circ}$]	24	Angle of attack
Δv [km s^{-1}]	200	Velocity range of emission spectra with pixel size $\delta v = 2 \text{ km s}^{-1}$.
$M_w(\text{H I}) [M_{\odot}]$	10^7	Stream neutral (initial) gas mass

NOTE. — ^a See Table 2. ^bThe exact value will vary by small factors depending on T_h (see equation 14).

Only gas clouds that are not overly dense and which have low pressure support with respect to the ambient medium will be disrupted in realistic time scales of ~ 100 Myr (Bland-Hawthorn 2009). We adopt $\eta = 100$ and $\xi = 0.1$. With these parameters fixed, the initial temperature of the warm gas phase is set by the temperature of the hot gas phase through

$$T_w = \left(\frac{\mu_w}{\mu_h}\right) \left(\frac{\xi}{\eta}\right) T_h, \quad (14)$$

where it should be noted that the mean molecular weight is generally different in each phase.

A key parameter of the models is the normalization of the density profile at the *canonical* distance of the Stream above the SGP ($d = 55$ kpc). Although still uncertain, different lines of evidence indicate that it is likely on the order of 10^{-4} cm^{-3} at $10 \text{ kpc} \lesssim r \lesssim 100 \text{ kpc}$ (e.g. Bregman & Lloyd-Davies 2007; Grcevich & Putman 2009; Gatto et al. 2013). We adopt a fiducial value $n(55 \text{ kpc}) = 10^{-4} \text{ cm}^{-3}$, independent of τ . This value is lower by roughly a factor two with respect to the value adopted by Bland-Hawthorn et al. (2007). However, we choose such a conservative value, since higher densities would enhance the warm cloud’s disruption through the growth of Kelvin-Helmholtz (KH) modes operating on time scales $\tau_{\text{KH}} \propto \eta^{1/2}$ (q.v. Appendix E), which in turn would enhance the shock cascade and the resulting $\text{H}\alpha$ emission.

We run all simulations in a cubic box of comoving size $18 \times 9 \times 9 \text{ kpc}^3$, using a (fixed) grid composed of $432 \times 216 \times$

⁵ This value is conservative in the sense that a higher metallicity would enhance cooling of gas, which in turn would yield a higher predicted $\text{H}\alpha$ emission (see Section 4).

216 cells. These measures imply a spatial resolution of $\delta x = (9/216) \text{ kpc} \approx 42 \text{ pc}$. The fragment of gas representing the Magellanic Stream is initially constrained to a cylinder 18 kpc in length and 2 kpc in diameter, and whose axis of symmetry runs parallel to the x axis of the coordinate system defined by the box. The angle of attack is defined with respect to the x -axis of this cylinder. In this setup, the x -axis coincides with the Magellanic longitude, l_M , whereas any of y or z run along the Magellanic latitude, b_M (Wakker 2001; Nidever et al. 2008). The simulated Magellanic Stream consists of an H I gas distribution initially at temperature $T_w \sim 10^3 \text{ K}$ (see equation 14); a mean (initial) hydrogen particle density $n \sim 10^{-3} \text{ cm}^{-3}$; and a total (neutral) gas mass $M_w(\text{H I}) \sim 10^7 M_{\odot}$. The initial warm gas density field corresponds to the density of a fractal medium described by a Kolmogorov turbulent power spectrum $P(k) \propto k^{-5/3}$, with a minimum wavenumber $k_{\text{min}} = 8$ (relative to the grid) corresponding to a spatial scale of 2.25 kpc (q.v. Sutherland & Bicknell 2007), comparable to the typical size of clouds in the Stream. The H I gas cloud is assumed to be at a given (fixed) distance r_{MS} from the Galactic Centre in the direction of the SGP. The temperature T_h and the density n of the hot wind are set according to the value of τ and the distance r_{MS} as given by equations (9) and (11), respectively.

For each $\tau \in \{0.5, 0.75, 1.0\}$, we consider a set of Galactocentric distances $r_{\text{MS}} \in \{55, 75, 100, 125, 150\} \text{ kpc}$ which together span the range of plausible orbits of the MS above the SGP. This yields 15 models. Each model is run for a total (simulation) time of 320 Myr, starting from $t_{\text{sim}} = 0 \text{ Myr}$, assuming free boundary conditions. The simulation output for a given set of values $\{\tau, r_{\text{MS}}, t_{\text{sim}}\}$ – in steps of $\Delta t_{\text{sim}} = 10 \text{ Myr}$ – consists of a series of datacubes containing information about the H I- and H II densities, $n_{\text{H I}}$ and $n_{\text{H II}}$, respectively; the gas temperature T , and the gas velocity $\vec{v} = (v_x, v_y, v_z)$. Using this information, we compute the $\text{H}\alpha$ and the H I 21 cm intensity of each cell, and from these the $\text{H}\alpha$ surface brightness and H I 21 cm emission of each snapshot. We refer the reader to Appendix D for a detailed description.

3.3. Emission line spectra

We compare the $\text{H}\alpha$ emission of the gas in our simulations to hi- and low-resolution Fabry-Pérot $\text{H}\alpha$ observations along the Magellanic Stream presented in the literature (Putman et al. 2003; Bland-Hawthorn et al. 2013), and complement these with results on the predicted properties of the respective H I 21 cm emission. Given the one-to-one correspondence between the H I 21 cm emission (i.e., brightness temperature) T_B and the H I column density of a parcel of optically thin gas (q.v. Dickey & Lockman 1990), we use the H I column density ($N_{\text{H I}}$) as a proxy for the corresponding H I 21 cm emission, which is simply obtained by integrating $n_{\text{H I}}$ along the sightline, and, for convenience, we *define* the H I 21 cm intensity to be $I_{\text{H I}} \equiv N_{\text{H I}}$.

The $\text{H}\alpha$ emission is computed using

$$\mu_{\text{H}\alpha} = \mu_{\text{H}\alpha}^{(\text{shock})} + \mu_{\text{H}\alpha}^{(\text{phot})}. \quad (15)$$

The first term accounts for the ionization that results from the shock cascade and the interaction with the hot halo (Bland-Hawthorn et al. 2007), and is given by (q.v. Appendix D)

$$\mu_{\text{H}\alpha}^{(\text{shock})} = 1.09 K_R \alpha_B^{(\text{H}\alpha)}(T) \int (n_{\text{H II}})^2 ds, \quad (16)$$

where $K_R \approx 1.67 \times 10^{-4} \text{ cm}^2 \text{ s mR}$,⁶ and the numerical factor 1.09 roughly accounts for the conversion of electron density to H II particle density (assuming $n_{\text{H}}/n_{\text{He}} \approx 0.1$ and single-ionized helium). The second term in equation (15) accounts for the ionizing effect of the cosmic ultra-violet background radiation (UVB). The H α emission along the sightline of gas in photoionisation equilibrium with the UVB radiation field is

$$\mu_{\text{H}\alpha}^{(\text{phot})} = \frac{1}{4\pi} \Gamma_{\text{H I}} \int (f_{\text{H}\alpha} n_{\text{H I}}) ds. \quad (17)$$

where $f_{\text{H}\alpha}(T)$ gives the fraction of recombinations that produce an H α photon, and $f_{\text{H}\alpha}(10^4 \text{ K}) \approx 0.45$ (equation D16). the H I recombination rate, $\Gamma_{\text{H I}}$, is related to the total ionizing photon flux (in photons $\text{cm}^{-2} \text{ s}^{-1}$) through

$$\Phi_i = \frac{\gamma + 3}{4\gamma} \sigma_0^{-1} \Gamma_{\text{H I}} = \frac{2}{3} \sigma_0^{-1} \Gamma_{\text{H I}}, \quad (18)$$

Here, $\sigma_0 = 6.3 \times 10^{-18} \text{ cm}^2$ is the hydrogen ionization cross section at the Lyman limit, $\nu_{\text{L I}} \approx 3.29 \times 10^{15} \text{ Hz}$. We adopt $\Gamma_{\text{H I}} = 10^{-13} \text{ s}^{-1}$ and $\gamma = 1.8$ (Weymann et al. 2001; Shull et al. 1999), corresponding to an ionizing flux $\Phi_i \sim 10^4 \text{ photons cm}^{-2} \text{ s}^{-1}$. To mimic radiation transfer effects, we limit the depth (along the sightline in any direction) of the gas ionized by the UVB to a maximum value defined by the condition that the column recombination ($n_e n_{\text{H II}} \alpha_B$) equals the incident ionizing photon flux (Φ_i). This condition is equivalent to restricting the ionizing effect of the UVB to a column of neutral gas $\sim 10^{17} \text{ cm}^{-2}$ (see Appendix D.3 for more details). The effect of the cosmic UVB is to produce an ionization skin around the cloud featuring an H α surface brightness at a level of roughly 5 mR. Note that this approach is not entirely self-consistent with our simulations because the ionizing effect of the UVB is not included at runtime, and because it assumes photoionisation equilibrium. Also, we ignore for the moment the contribution of the Galactic ionizing field, which would produce an additional mean H α signal of $21 \zeta (d/55 \text{ kpc})^{-2} \text{ mR}$ ($\zeta \approx 2$; Bland-Hawthorn et al. 2013).

To allow for a faithful comparison with observations, we map the simulation data onto observed space by projecting the simulation volume along a given axis, so as to mimic the projection of the observed emission along the Stream onto the plane of the sky. We choose, for convenience, an axis parallel to one side of the simulation box, and perpendicular to the Stream's main axis. Each sightline across the projected datacube corresponds to a pencil-beam spectrum. H α and H I 21 cm pencil-beam spectra along the chosen projection axis are constructed by computing the intensity for each cell in the simulation volume according to equation (D9). We adopt a spectral range in terms of velocity of $\Delta v = 200 \text{ km s}^{-1}$ which corresponds to the spectral range provided by the WHAM spectrometer. The velocity scale is given with respect of the initial rest-frame of the H I gas, such that emission spectrum spans the range $[-100, +100] \text{ km s}^{-1}$, with a pixel size $\delta v = 2 \text{ km s}^{-1}$.

At each beam position (or 'pointing'), we compute the intensity-weighted average of all cells within the beam, resulting in a single 'beam spectrum' per pointing. We consider both a low resolution beam, corresponding to the 1° diameter beam on the sky provided by the WHAM spectrometer; and a high resolution beam with a diameter of $10'$ which is comparable

⁶ 1 milli-Rayleigh (mR) corresponds to $10^3/4\pi \text{ photons cm}^{-2} \text{ s}^{-1} \text{ sr}^{-1}$, or $2.41 \times 10^{-4} \text{ erg cm}^{-2} \text{ s}^{-1} \text{ sr}^{-1}$ at H α .

to the resolution of the TAURUS-2 Fabry-Pérot interferometer (Putman et al. 2003).

We choose a rectangular (rather than a circular) beam, which allows for a full coverage of the projected image, and which greatly simplifies the scanning procedure.⁷

Given that a beam with a diameter of 2θ subtends a solid angle $\Omega_{\text{beam}} \approx \pi (\theta/2)^2$ (provided that $\theta \ll 1$), the linear size of a square subtending a solid angle Ω_{beam} at a distance r_{MS} relative to the angular dimension of a single cell in our simulation, $\delta\Omega_V \approx (\delta x / r_{\text{MS}})^2$, is roughly given by

$$\delta l = \left(\frac{\Omega_{\text{beam}}}{\delta\Omega_V} \right)^{1/2} = \left(\frac{\pi}{4} \right)^{1/2} \frac{r_{\text{MS}}}{\delta x} \theta. \quad (19)$$

The emission within a beam pointing at each velocity v_m , i.e. the beam spectrum, is⁸

$$\bar{I}_X = [\delta l]^{-2} \sum_{[\delta l]} \sum_{[\delta l]} I_X, \quad (20)$$

where the sum extends over all cells within Ω_{beam} , and $X \in \{\text{H I}, \text{H II}\}$. Here, the notation $[k]$ indicates the largest odd integer smaller than or equal to k . The last equality follows from the fact that every cell in the simulation volume subtends the same solid angle $\delta\Omega_V$ (at a given distance). The average of the emission within each beam pointing can effectively be obtained by overlaying a rectangular grid on the projected image with a cell size equal the solid angle subtended by a circular beam of diameter 1° ($10'$) at that distance, and computing the arithmetic mean within each new cell. We choose the origin of the matrix to be shifted by half a beam size in each direction (xy) to avoid the uncertainties associated with the simulation volume's boundaries.

It is important to emphasize that the pixelation of the simulation volume and the position of the beam pointings with respect to the projected datacube are rather arbitrary. Also, the latter is also generally different for each adopted Stream distance r_{MS} . This results from the fact that for a computational volume with fixed comoving size and fixed grid, and a beam of fixed angular size, an increasing fraction of the gas that represents the Stream will be sampled by the beam with increasing distance (Table 4). Because of this, and also to avoid a bias in the resulting emission introduced by potentially bright features induced by chance alignments (rather than due to intrinsically bright gas blobs), *prior* to computing the spatial average within each beam pointing we smooth each 2D spatial slice at each velocity bin using a circular Gaussian kernel with a full width at half maximum of half the beam size (e.g. FWHM = 0.5°) and a total width of (i.e., truncated at) the size of the beam (e.g. 1°). According to the approach described above, the projected (intrinsic) H α emission map from our simulation is smoothed at each given distance using a Gaussian kernel with FWHM of $[\delta l/2]$ pixel and a total width of $[\delta l]$ pixel.

Finally, in order to take into account the instrumental line broadening, we convolve each spatially averaged spectrum

⁷ A alternative arrangement consisting of a tightly packed array of circular windows (which conveys equal weight to every pixel within the beam; see e.g., Haffner et al. 2003, their Figure 3) would yield essentially the same results.

⁸ Note that if all pixels within a pointing have the same intensity, and for simplicity, $[\delta l] \equiv \delta l$, then

$$\bar{I}_X = [\delta l]^{-2} \sum_{[\delta l]} \sum_{[\delta l]} I_X = [\delta l]^{-2} I_X [\delta l]^2 = I_X.$$

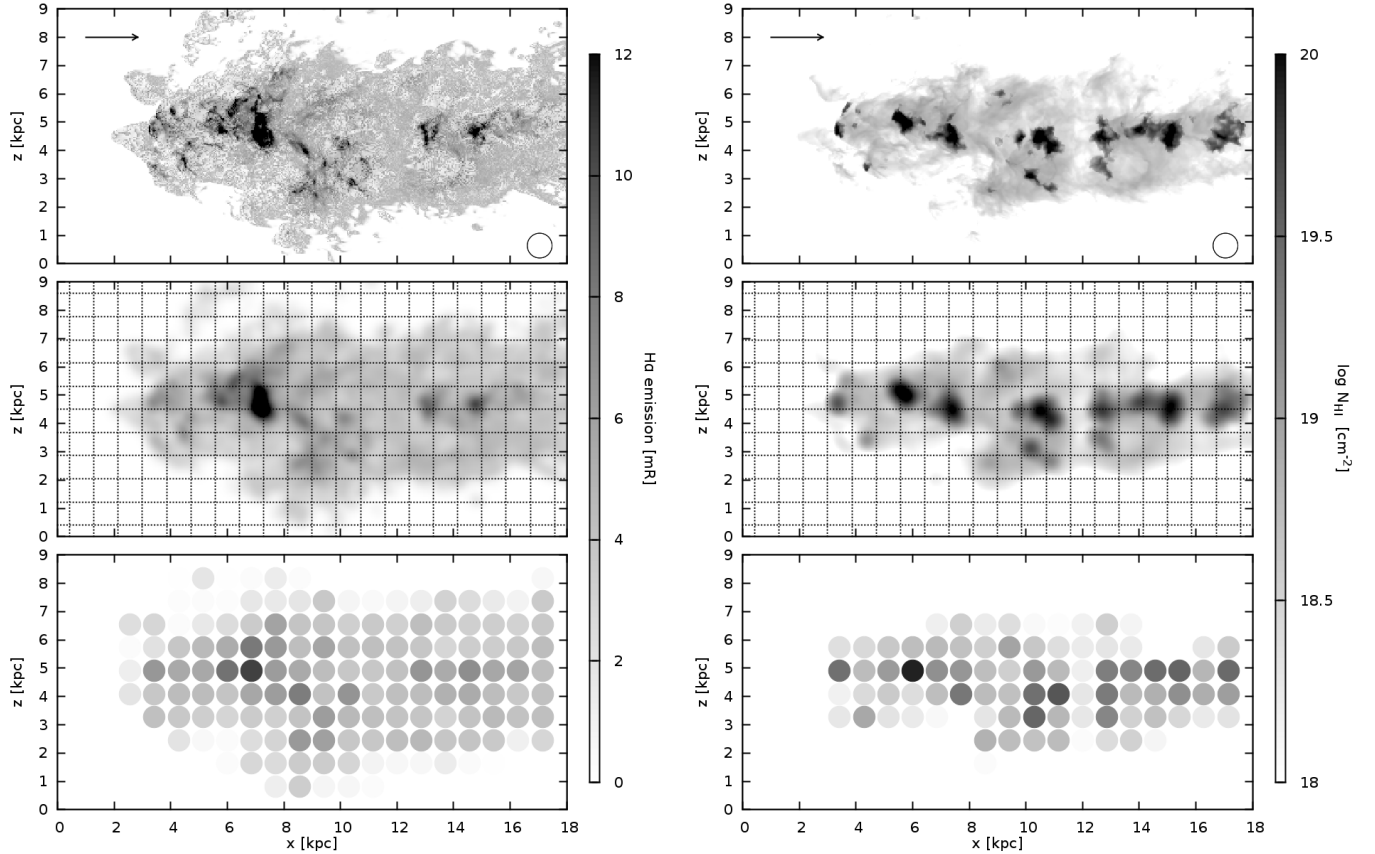


FIG. 3.— Virtual observation of the $H\alpha$ (left) and $H\text{ I } 21\text{ cm}$ (right) emission along the Stream in model $\tau = 0.75$ and $r_{\text{MS}} = 55\text{ kpc}$ at $t_{\text{sim}} = 170\text{ Myr}$, projected along the y axis. Top: Emission at the intrinsic (high) resolution of the simulation. The arrow on the top-left corner indicates the projected wind velocity. Middle: The result of spatially smoothing the emission map using a circular Gaussian kernel of size $0.5^\circ / 1^\circ$ (FWHM / full width), as indicated by the circle on the bottom-right corner of the top panel. Bottom: Emission at different pointings obtained using a beam with an angular diameter of 1° on the sky. The position of each individual pointing is defined by each cell of the grid overplotted on the middle panel. The grayscale bar to the right of each column indicates the $H\alpha$ intensity in milli-Rayleigh (left) and the $H\text{ I}$ column density in cm^{-2} (right). (This figure is also available in color, and different projections, resolution, and Stream distances; see Appendix F.)

using a Gaussian kernel⁹ with a FWHM = 12 km s^{-1} , which roughly corresponds to the resolution of the WHAM spectrograph (Reynolds et al. 1998). The $H\alpha$ surface brightness and $H\text{ I } 21\text{ cm}$ emission maps are simply obtained from the 3D spectral datacube by simply integrating each spectrum along the velocity coordinate (equation D10).

A selected example illustrating the result of the above procedure is shown in Figure 3 (see also Figures 6, 11, and 12). As we show below (see Section 4.3, Figure 7), the $H\text{ II}$ to $H\text{ I}$ mass ratio in this snapshot roughly matches to the corresponding ratio observed in the Magellanic Stream (~ 3 ; Fox et al. 2014). The effect of the ionizing cosmic UVB is apparent: all the Stream gas is lit up and emitting at level of $\sim 5\text{ mR}$. But there are brighter spots which are a consequence of the shock cascade, whereby the trailing clouds collide with the material ablated by hydrodynamic instabilities from the leading gas, thus being shock ionized (q.v. Bland-Hawthorn et al. 2007). Interestingly, while the bright $H\alpha$ spots seem to closely track the high $N_{\text{H I}}$ parcels of gas, the converse is not true, with high $N_{\text{H I}}$ appearing with no correspondent strong $H\alpha$ emission. However, these

⁹ Note that the LSF of the WHAM spectrometer is only poorly approximated by a Gaussian (Tufté 1997). However, given the typical $H\alpha / H\text{ I } 21\text{ cm}$ line widths ($20\text{ km s}^{-1} - 40\text{ km s}^{-1}$), this approximation hardly affects our results.

TABLE 4
ANGULAR AND SPATIAL RESOLUTION

r_{MS} [kpc]	$[\delta l]_{1^\circ}$	Size [kpc]	$[\delta l]_{10'}$	Size [kpc]
55	21	0.9	3	0.1
75	27	1.1	5	0.2
100	37	1.5	7	0.3
125	47	2.0	7	0.3
150	55	2.3	9	0.4

NOTE. — This table lists the linear dimension of a rectangular beam (equivalent to a circular beam subtending the same solid angle) in units of the comoving (linear) cell size, δx , and in kpc, as a function of Galactocentric distance r_{MS} for beams with diameter 1° and $10'$ (see equations 19 and 20).

differences become less apparent, although they remain, as a result of the beam smearing. The most dramatic effect of the latter is the dilution of the $H\alpha$ and $H\text{ I}$ signals with respect to the brightest levels seen at the (intrinsic) resolution of the simulation by a significant factor. Only the brightest spots in $H\alpha$ would be observable with a Fabry-Pérot interferometer, or in $H\text{ I}$ with a radio telescope, for reasonable integration times, leading to a significant fraction of the gas mass falling below the detection threshold.

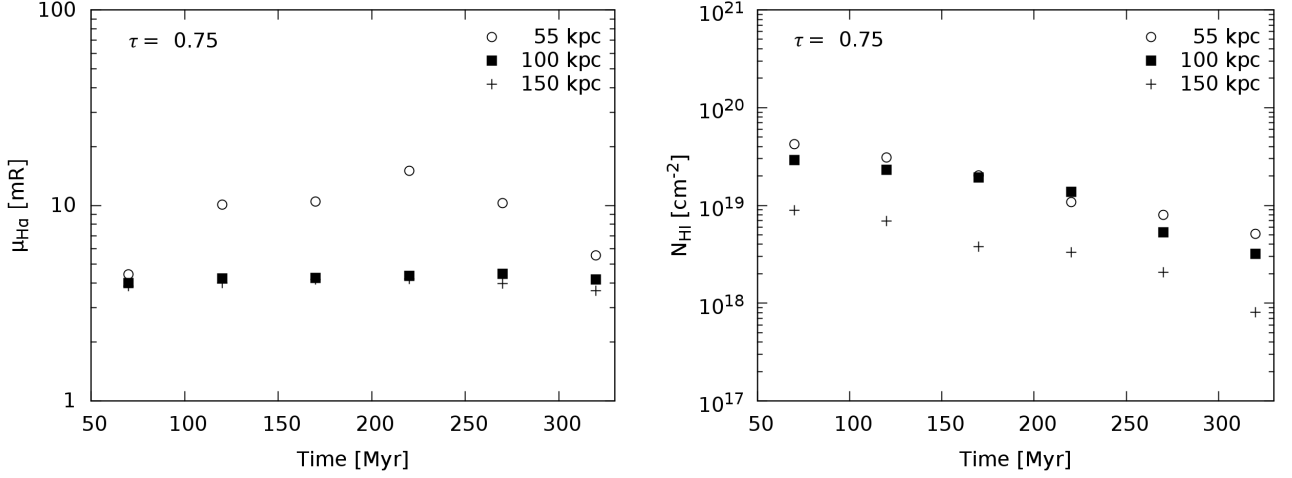


FIG. 4.— Evolution of the $H\alpha$ surface brightness (left) and the $H\text{ I}$ column density (right). For a given time, the data points correspond to the 90 percentile of the distribution of observed values, assuming the MS to be at a Galactocentric distance $r_{\text{MS}} = 55$ kpc (circle), 100 kpc (square), and 150 kpc (cross). The results are essentially the same for $\tau = 0.5, 1.0$, and 1.5 , and are therefore not shown.

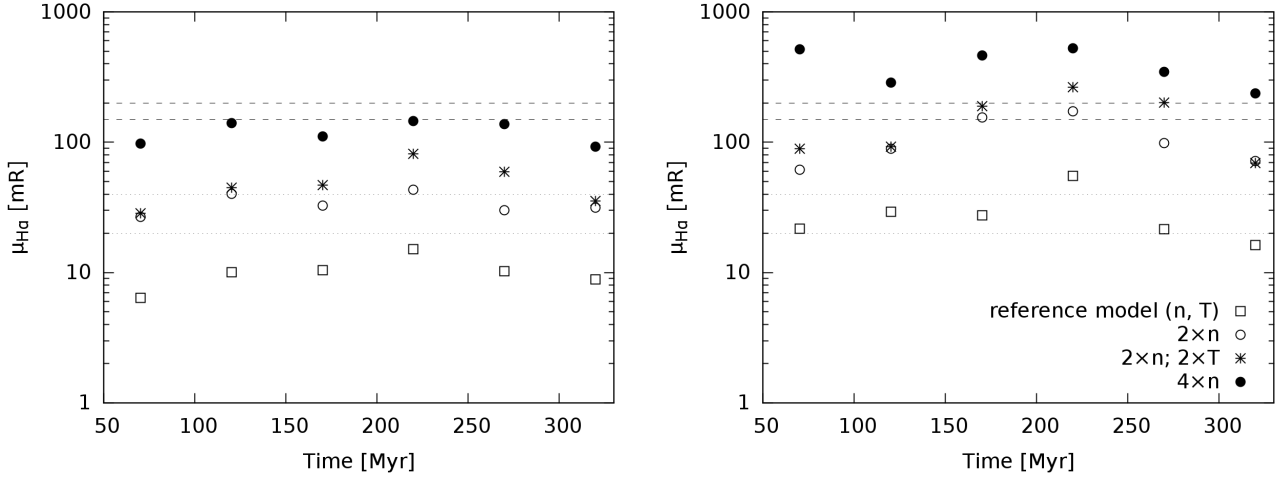


FIG. 5.— Evolution of the *peak* (short-lived) $H\alpha$ surface brightness for low (left) and high (right) resolution observations in the reference model and variations thereof. The ‘reference model’ corresponds to the model defined by the set of parameter values $\{\tau, r_{\text{MS}}, n(55 \text{ kpc}), T_h\} = \{0.75, 55 \text{ kpc}, 10^{-4} \text{ cm}^{-3}, 8 \times 10^5 \text{ K}\}$. The set of dotted and dashed horizontal lines indicate, respectively, the range in the $H\alpha$ emission induced by the Galactic UV radiation field at $d = 55$ kpc (Bland-Hawthorn & Maloney 2002), and the range of mean $H\alpha$ detections observed along the Magellanic Stream (Bland-Hawthorn et al. 2013).

4. RESULTS

4.1. Integrated gas emission

We follow the evolution of the gas emission over a period of 330 Myr in all 15 models. To illustrate these results, we present in Figure 4 the evolution of the $H\alpha / H\text{ I}$ emission for model $\tau = 0.75$, and three representative distances $r_{\text{MS}} = 55$ kpc, 100 kpc, and 150 kpc. The results are essentially the same for $\tau = 0.5, 1.0$, and 1.5 , and are therefore not shown. Quite surprisingly, the $H\alpha$ emission along the model Stream never exceeds 20 mR. Note that this level of emission is comparable to, or even less significant than, the emission induced by the Galactic ionizing starlight (20 – 40 mR [$d/55$ kpc]). This is chiefly the reason for us ignoring this component in our models. The highest $H\alpha$ emission is observed at the lowest Galactocentric distance of $r_{\text{MS}} = 55$ kpc, as expected, since the halo gas density is highest at this distance. The emission at distances $r_{\text{MS}} \gtrsim 100$ kpc is dominated by the contribution of the cosmic UV background to the gas ionization. Note that often we do find spots along the Stream with $\mu_{H\alpha} > 10$ mR in our simulation, and rarely on

the order of ~ 100 mR, but their strong signal is washed out as a result of the beam smearing (see also Figures 3, 11, 12).

The $H\text{ I}$ column density decreases uniformly both with time (as expected due to the increasing ionization of the gas), and with distance, as a consequence of beam dilution (see also Figure 12). The gas giving rise to the optical emission ionizes quickly (~ 100 Myr), after which peak $H\alpha$ emission remains remarkably constant around ~ 10 mR. Given that observations performed with the WHAM instrument typically reach a sensitivity of $\gtrsim 30$ mR, the Stream in our models would be essentially undetectable (again, ignoring the contribution which results from the Galactic ionizing field). In contrast, the gas would be relatively bright in $H\text{ I}$ 21 cm, considering that the sensitivity of e.g the LAB survey is roughly $N_{H\text{ I}} = 5 \times 10^{18} \text{ cm}^{-2}$, up to ~ 250 Myr, after which it falls below the detection threshold.

It is clear that a higher halo density (or equivalently, a smaller Stream distance) should enhance the onset and development of KH instabilities, thus promoting the shock cascade and the associated $H\alpha$ emission. Also, a brightly emitting spot with a characteristic size significantly smaller than the beam size

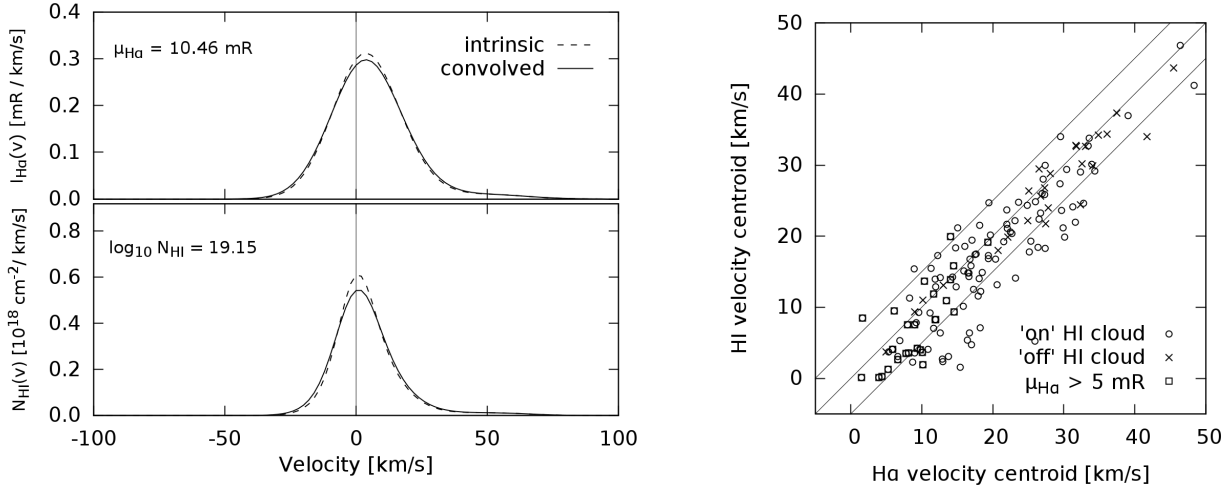


FIG. 6.— Gas kinematics in model $\tau = 0.75$ and $r_{\text{MS}} = 55$ kpc at $t_{\text{sim}} = 170$ Myr. Left: Emission spectra observed at the pointing with the brightest $\text{H}\alpha$ emission shown in the bottom panel of Figure 3. We show for comparison the intrinsic line profile and the line profile convolved with a Gaussian LSF with a FWHM = 12 km s^{-1} . Right: Line-of-sight velocity centroid of the $\text{H}\alpha$ intensity detected ‘on’ and ‘off’ H I clouds (see text for details). The solid diagonal lines indicate the identity line and a $\pm 5 \text{ km s}^{-1}$ range around this line.

will unavoidably be observed to be much dimmer, or perhaps even fall below the detection threshold. Indeed, the brightest $\text{H}\alpha$ observations along the Stream have been obtained with high resolution ($10'$) interferometers. Table 4 shows that, for example, a beam of 1° diameter samples a region of twice the size at $r_{\text{MS}} = 100$ kpc with respect to $r_{\text{MS}} = 55$ kpc. A beam with a diameter of $10'$ samples a region which is nearly ten times smaller than a 1° beam at $r_{\text{MS}} = 55$ kpc (see also Figure 12).

In order to explore the effect of different beam sizes, we consider two different (low / high) resolutions for the model defined by the set of parameter values $\{\tau, r_{\text{MS}}, n(55 \text{ kpc}), T_h\} = \{0.75, 55 \text{ kpc}, 10^{-4} \text{ cm}^{-3}, 8 \times 10^5 \text{ K}\}$ (the ‘reference model’). We also explore the effect of higher halo densities and temperatures. The results are presented in Figure 5, which shows the evolution of the *peak* (and short-lived) $\text{H}\alpha$ emission of the gas. As expected, a denser halo aids the production of $\text{H}\alpha$ emission through stronger hydrodynamical interactions, but the emission appears to be rather insensitive to the value of the temperature (as long as it does not varies by orders of magnitude). Also, a higher resolution beam results in stronger detected emission levels, as a consequence of the less dramatic beam dilution.

4.2. Gas kinematics

The kinematics of the warm neutral and ionized gas phases as traced by $\text{H}\alpha$ and H I 21 cm emission provide a insight into the mechanism ionizing the Stream. We explore this using the spectra of our model identified by $\tau = 0.75$ and $r_{\text{MS}} = 55$ kpc at $t_{\text{sim}} = 170$ Myr. Note that the results, with exception of the $\text{H}\alpha$ emission strength, are virtually identical for all other models. An example of a strong $\text{H}\alpha$ and H I 21 cm emission lines is shown in the top panel of Figure 6. These correspond to the pointing with the brightest $\text{H}\alpha$ emission shown in the bottom panel of Figure 3. The integrated strength of the line is indicated in each case in the top-left corner. For reference, the typical sensitivity of WHAM (30 mR) translates into a spectral sensitivity of $0.5 \text{ mR} / \text{km s}^{-1}$, assuming a typical line width of 30 km s^{-1} . Similarly, the sensitivity of the LAB survey ($N_{\text{HI}} = 5 \times 10^{18} \text{ cm}^{-2}$) corresponds to a spectral sensitivity of $10^{17} \text{ cm}^{-2} / \text{km s}^{-1}$. Thus, while the $\text{H}\alpha$ emission in this case

falls well below the WHAM detection threshold, the H I 21 cm feature shown in this Figure would be comfortably detected in a survey similar to LAB. We find typical line widths of $20 - 30 \text{ km s}^{-1}$ (FWHM), which are consistent with observations (Putman et al. 2003).

We study the difference in the kinematics of the warm neutral and ionized gas by comparing the sightline velocity centroid of the $\text{H}\alpha$ emission to the H I 21 cm emission, distinguishing between pointings ‘on’ and ‘off’ the H I clouds. In this context, ‘on’ (‘off’) means that the H I 21 cm emission is above (below) $N_{\text{HI}} = 5 \times 10^{18} \text{ cm}^{-2}$. In addition, we flag those pointings where the $\text{H}\alpha$ emission is above the level expected from ionization by the UVB (Figure 6, bottom panel). We do not find a significant difference between the sightline velocities of the warm neutral and ionized gas phases; their respective velocity centroids agree within $\pm 5 \text{ km s}^{-1}$, as observed (Putman et al. 2003; Barger et al. 2015). We find virtually no $\text{H}\alpha$ emission ($\mu_{\text{H}\alpha} < 5 \text{ mR}$) detached from (significant) H I 21 cm emission. Also, the velocity of this strong $\text{H}\alpha$ emission is generally low ($v \lesssim 20 \text{ km s}^{-1}$), with a tendency for the strongest emission to have the lowest velocities indicating that it is truly associated to the H I gas. This coincidence in both velocity and physical space of the $\text{H}\alpha$ / H I signal is a characteristic signature of the shock cascade. The fact that the strength of the $\text{H}\alpha$ emission observed along the Magellanic Stream greatly exceeds the emission we obtain from our models, suggests that a mechanism other than a shock cascade must be operating along the Stream.

4.3. Gas ionization time scales

It has recently been inferred that the mass of the ionized gas kinematically associated to the Magellanic Stream is roughly 3 times larger than its H I mass (Fox et al. 2014). Here, we briefly explore the evolution of the ionized and warm-neutral gas mass fractions, using the H II and H I masses in as a proxy for the ionized and warm-neutral gas phases, respectively. Again, we focus on the results obtained from our models characterized by $\tau = 0.50, 0.75, 1.00$ and $r_{\text{MS}} = 55$ kpc. Note that the results are qualitatively the same for all other models. Figure 7 shows the evolution of the individual mass fractions $f_X \equiv M_X / M_{\text{tot}}$, where $X \in \{\text{H I}, \text{H II}\}$ and $M_{\text{tot}} = M_{\text{H I}} + M_{\text{H II}}$, as well as the

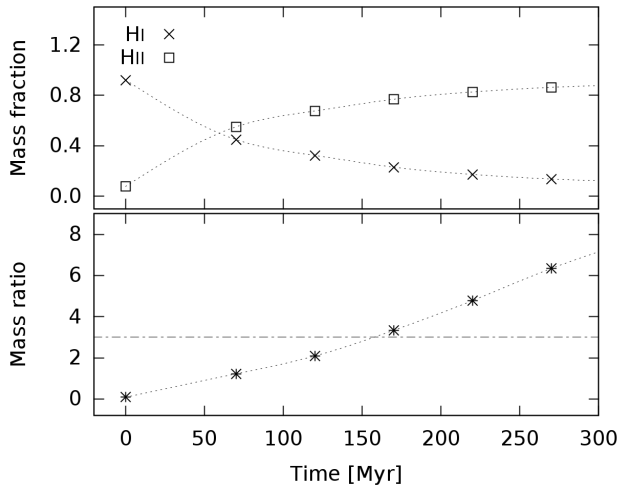


FIG. 7.— Evolution of the H I and H II mass fractions in the $\tau = 0.75$ model Stream at $r_{\text{MS}} = 55$ kpc, projected along the y -axis. The top panel shows the evolution of the individual mass fractions M_X/M_{tot} , where $X \in \{\text{H I}, \text{H II}\}$ and $M_{\text{tot}} = M_{\text{H I}} + M_{\text{H II}}$. The bottom panel shows the evolution of the H II to H I mass ratio. The dashed horizontal line indicates the ratio H II : H I = 3 inferred from observations (Fox et al. 2014). Note that the model series have been joined to guide the eye only. The results are essentially the same for $\tau = 0.5$, 1.0, and 1.5, and are therefore not shown.

evolution of the H II to H I mass ratio. We include for reference the inferred value of the ratio H II : H I = 3. We find that the gas evolves on a typical time scale of 100 Myr, which is consistent with the time estimate which results from assuming that the cloud disrupt by the action of Kelvin-Helmholtz instabilities and our adopted (initial) value of η . After this period, the ionization effect of the halo-cloud and cloud-cloud interaction leads to a reduction of the warm neutral gas mass by half. The H II : H I mass ratio increases rapidly with time, and the inferred H II : H I mass ratio of 3 is reached after ~ 170 Myr.

Since our simulations assume free boundary conditions, it is difficult to quantify with precision how much of the neutral gas is ionized and how much simply escapes the simulation volume. Nonetheless, we estimate that only a negligible fraction of the warm-neutral gas is lost by $t_{\text{sim}} \lesssim 270$ Myr. Therefore, the ionization of the gas due to interactions with the hot halo gas, and due to cloud-cloud interactions lead to a strong evolution of the mass fractions in the neutral and ionized phases. The relatively short survival time scale implies the requirement for a continuous replenishment of gas from the MC to the Stream (Bland-Hawthorn et al. 2007).

We find that much of the gas dislodged from the main body of the Stream is low density material that mixes rapidly with the halo gas, thereby being heated (and thus ionized) to temperatures well above 10^5 K, which are on the order of the temperature expected for turbulent mixing (Begelman & Fabian 1990). At these temperatures, the $\text{H}\alpha$ emissivity drops by nearly two orders of magnitude with respect to its value 10^4 K (Figure 10), and the ionized gas becomes thus practically invisible in $\text{H}\alpha$. Only the gas ionized by cloud-cloud collisions remains at relatively low temperatures ($\sim 10^4$ K), and thus provides the strongest $\text{H}\alpha$ signal. However, the fraction of warm ionized gas is very low overall, and thus is the corresponding $\text{H}\alpha$ signal. In other words, only a mechanism able to ionize a significant fraction of the gas without increasing its temperature far above 10^4 K will lead to significant $\text{H}\alpha$ emission.

5. DISCUSSION

We have shown that the interpretation of the mean optical emission observed along the Magellanic Stream ($\approx 100 - 200$ mR) as a result of a slow shock cascade fails unless the coronal density surrounding the Stream is significantly higher than expected. This would require either that the coronal density model is seriously wrong or that the Stream is much closer than the Magellanic Clouds ($d < 20$ kpc) at which point the Galactic UV intensity would also contribute to the gas ionization. However, both possibilities are ruled out by a number of observations.

First, the absence of absorption in the spectra of halo stars with velocities consistent with Magellanic Stream gas puts a lower limit on the Stream’s distance $d > 20$ kpc (Lehner & Howk 2011; Lehner et al. 2012), although the evidence is somewhat circumstantial. Similarly, a lower limit is set by the fact that the Stream originates somewhere in the Magellanic Cloud system. The distance modulus of the LMC is known to within 3 percent, with a mean value $(m - M)_0 = 18.48$ mag, which corresponds to a distance of 49.7 kpc (Walker 2012). The Araucaria Project has determined the distance modulus of the SMC to similar precision, with a mean value of 18.965 mag, which translates into a distance 62.1 ± 1.9 kpc (Graczyk et al. 2014). It is therefore unlikely that the Stream lies at $d < 55$ kpc, at its origin, and even less likely that it does so at the SGP, given the substantial eccentricity of the LMC and SMC orbits (Besla et al. 2012). We may use our models to put a limit on the minimum distance to the Stream. Indeed, our results indicate that if the Stream was any closer than $d \approx 20$ kpc, the combined effect of the shock cascade and the Galactic UV ionizing field would light up the gas beyond the levels observed. This is independent of our halo model and relies only on the assumption that the coronal density increases by factors of a few with respect to $d = 55$ kpc, which is reasonable. We may also put a weak constraint on the maximum distance. Indeed, if the Stream was too far away, then it would be too massive ($M \propto d^2$). The limit on the mass on the Stream is set by the combined amount of neutral and ionized mass in gas that the MCs may deliver, which is on the order of $10^9 M_\odot$. The most recent estimate of the Stream’s mass $\sim 2 \times 10^9 M_\odot [d/55 \text{ kpc}]^2$ (Fox et al. 2014) supports the assertion that distances $d > 100$ kpc are rather unlikely.

Second, the density of the Galactic corona at $10 \text{ kpc} < d < 100 \text{ kpc}$ appears to be known to within a factor of a few, with a mean total particle density on the order of 10^{-4} cm^{-3} (e.g. Miller & Bregman 2015). These estimates are however model dependent, and they rely on uncertain assumptions about the metallicity and ionization state of the gas, and, more crucially, about the structure of the corona. The weakest of all is perhaps the assumption of a *smooth* corona. Here we have provided a self-consistent, working model for the Galactic corona which is well constrained by the properties of the Galaxy’s DM halo, but which relies as well on this very assumption. Within the framework of our model, it is possible to constrain the mean density of the halo at $d = 55$ kpc to $n \lesssim 2 \times 10^{-4} \text{ cm}^{-3}$ by requiring that the ratio of total gas mass enclosed within a given radius to the DM mass of the Galaxy does not exceed the cosmic fraction, both of which are well established (Kafle et al. 2014; Planck Collaboration et al. 2014). The upper bound on the density thus obtained is consistent with limits inferred from the scenario according to which the dwarf spheroidals orbiting the Galaxy have lost their gas as a consequence of the ram pressure exercised by the corona (Grcevich & Putman 2009;

Gatto et al. 2013). In view of this evidence, it seems unlikely that the *mean* density of the hot halo be above 10^{-4} cm^{-3} at 55 kpc. Incidentally, this circumstance, and the favorable comparison with two independent results (see Figure 2), argue against a serious flaw in our halo model.

Bland-Hawthorn et al. (2007) provide diagnostics of slow shocks (e.g. Balmer decrement) that are likely to be observable along the Magellanic Stream in future observing campaigns. If enhanced Balmer decrements ($H\alpha/H\beta \gtrsim 3$) are confirmed, then we must consider radical departures from our simple (smooth) halo model. One possibility is that the hot corona density distribution is asymmetric. While CDM accretion may be isotropic on average, individual events are not, as clearly demonstrated by the Magellanic Clouds. Also in the southern Galactic hemisphere, the Sgr dwarf extends through much of the halo (Ibata et al. 1994). The mass of this system was probably comparable to the LMC and may well have retained gas before being tidally disrupted. A more recent accretion event is attested by the massive H I stream, the Smith Cloud ($\gtrsim 2 \times 10^6 M_\odot$), that is presently being stripped and ablated by the corona (Lockman et al. 2008; Nichols et al. 2014). Hence, it is possible, even likely, that the hot corona is asymmetrically mass-loaded as a consequence of earlier accretion events, thus allowing for significant variations along different directions and at different radii, without violating constraints on, e.g. the total gas mass enclosed within r_{vir} .

To emphasize the reality and long-lived nature of coronal asymmetries, as well as their impact on the density distribution in the corona, we have run a test, full 3D `FYRIS ALPHA` simulation of a group of massive ($10^6 M_\odot$), warm (10^4 K) neutral HVCs plunging into the potential well of an isothermal DM halo ($10^{12} M_\odot$), filled with a hot (10^6 K) gas component ($10^{10} M_\odot$) initially in hydrostatic equilibrium with the potential. This is equivalent to having released eight Smith Clouds into the halo of the Galaxy as described by our model (Section 2). The top row in Figure 8 displays the initial (projected) distribution of neutral and ionized gas, while the subsequent panels show the neutral and ionized gas distributions after $\sim 1.5 \text{ Gyr}$ and $\sim 2 \text{ Gyr}$, respectively. While a rather crude model, it does illustrate the non-negligible effect of the anisotropic nature of accretion on the density profile of the corona. This experiment makes it clear that, in order to attain full consistency, the time variable nature of the halo needs to be taken into account. We will explore this in more detail in future work.

An important corollary of our models - which is an idea advanced by Bland-Hawthorn et al. (2007) - is that there is likely a significant (in terms of mass) amount of gas debris hidden in the hot halo. As we have shown, the Stream gas is broken down and quickly ionized due to both the interaction with the halo and cloud-cloud collisions. As a result, its neutral column density eventually falls below the detection threshold of current radio telescopes. In addition, the temperature of the gas is too high for the recombination emission to be important, and the interaction with the hot halo as well as the cloud-cloud collision leading to the shock cascade produce a rather weak optical emission. We estimate that the $H\alpha$ emission thus produced is comparable to the emission induced by the cosmic UVB at $d \approx 75 \text{ kpc}$, and the latter process dominates thereafter. At the same time, the temperature of the ablated Stream gas is not high enough for the associated X-ray emission to be observable. Hence, the ionized gas, whose mass increases substantially with time, is practically invisible to us in emission. But it may well be detected in absorption.

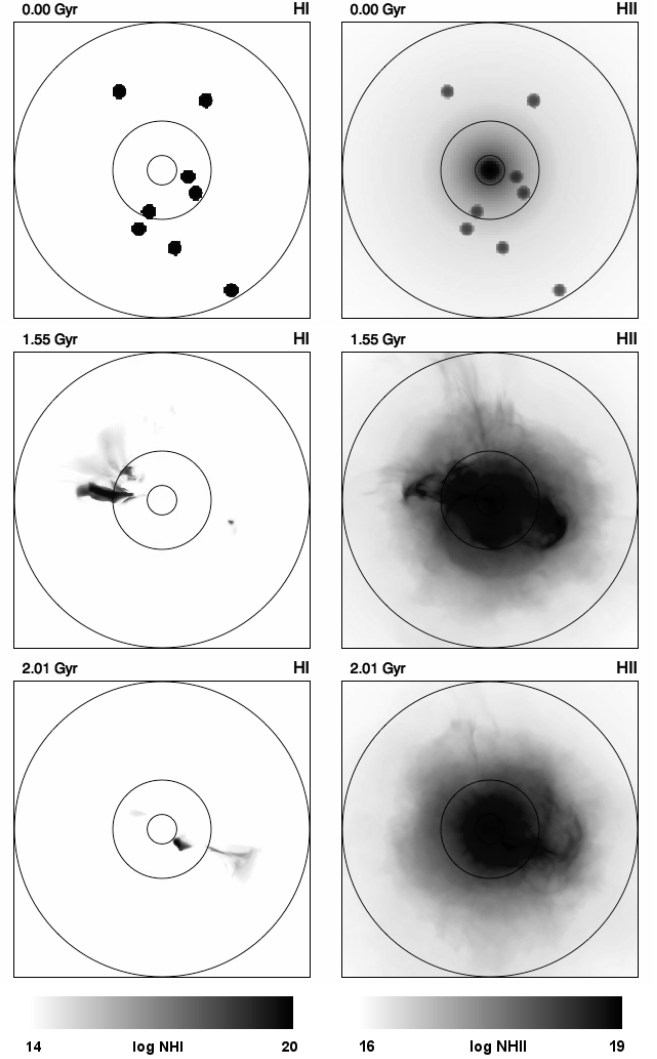


FIG. 8.— Evolution of the H I (left) and H II (right) gas distribution in a MW type halo. Each panel shows the column density projected along 100 kpc. The top row shows the initial (projected) position a group of massive ($10^6 M_\odot$), warm (10^4 K) neutral HVCs plunging onto the halo. The middle and bottom rows show the ionization state of the gas after $\sim 1.5 \text{ Gyr}$ and $\sim 2 \text{ Gyr}$, respectively. The concentric circles of increasing radius indicate a distance of 10 kpc, 30 kpc, and 100 kpc from the centre, and they are identical in all panels. Note the clear asymmetry in the hot (H II) gas distribution (left) between the initial and intermediate / final states. The mass-loading of the halo as a result of the accretion is also apparent.

As a matter of fact, several studies of the absorption signatures of gas detected against bright background sources have now found that the amount of ionized gas at velocities similar to spatially overlapping H I structures (e.g. Lehner & Howk 2011), in particular with the Magellanic Stream (Fox et al. 2014), is substantial.

To sum up, we have seen that it is difficult to explain the $H\alpha$ surface brightness levels over the SGP using newly updated parameters for the Galactic corona and the Stream’s distance. This model may still work if the hot corona is not smooth but filled with debris from recent accretion events, as we discuss above. An alternative model has recently been put forward in the context of the Galaxy’s nuclear activity. The energetic bubbles observed with the Fermi-LAT in gamma rays (Su et al.

2010) indicate that a powerful event has taken place at the nucleus in the recent past. If the gamma rays are produced through inverse Compton upscattering of soft photons, this event can be dated to 1-3 Myr ago (Guo & Mathews 2012). Within the context of this model, Bland-Hawthorn et al. (2013) show that the Stream H α emission can also be explained by accretion-disk driven ionization for Stream distances of 100 kpc or more over the poles. The recent discovery of high

ionization species (e.g. Si IV, C IV) over the SGP (Fox et al. 2015) may lend support to this model.

We thank Sebastián Nuza for providing the data from their simulation included in Figure 2 of this work. TTG acknowledges financial support from the Australian Research Council (ARC) through a Super Science Fellowship and an Australian Laureate Fellowship awarded to JBH.

REFERENCES

- Adams, J. J., Uson, J. M., Hill, G. J., & MacQueen, P. J. 2011, *ApJ*, 728, 107
 Asplund, M., Grevesse, N., Sauval, A. J., & Scott, P. 2009, *ARA&A*, 47, 481
 Baker, D. J., & Romick, G. J. 1976, *Appl. Opt.*, 15, 1966
 Baker, J. G., & Menzel, D. H. 1938, *ApJ*, 88, 52
 Barger, K., Madsen, G. J., Fox, A., et al. 2015, in *American Astronomical Society Meeting Abstracts*, Vol. 225, American Astronomical Society Meeting Abstracts, 253
 Begelman, M. C., & Fabian, A. C. 1990, *MNRAS*, 244, 26P
 Besla, G., Kallivayalil, N., Hernquist, L., et al. 2007, *ApJ*, 668, 949
 —. 2012, *MNRAS*, 421, 2109
 Bland-Hawthorn, J. 2009, in *IAU Symposium*, Vol. 256, IAU Symposium, ed. J. T. Van Loon & J. M. Oliveira, 122–128
 Bland-Hawthorn, J., & Maloney, P. R. 2002, in *Astronomical Society of the Pacific Conference Series*, Vol. 254, Extragalactic Gas at Low Redshift, ed. J. S. Mulchaey & J. T. Stocke, 267
 Bland-Hawthorn, J., Maloney, P. R., Sutherland, R. S., & Madsen, G. J. 2013, *ApJ*, 778, 58
 Bland-Hawthorn, J., Sutherland, R., Agertz, O., & Moore, B. 2007, *ApJ*, 670, L109
 Bregman, J. N., & Lloyd-Davies, E. J. 2007, *ApJ*, 669, 990
 Bregman, J. N., Otte, B., Irwin, J. A., et al. 2009, *ApJ*, 699, 1765
 Bryan, G. L., & Norman, M. L. 1998, *ApJ*, 495, 80
 Cavaliere, A., & Fusco-Femiano, R. 1976, *A&A*, 49, 137
 Dickey, J. M., & Lockman, F. J. 1990, *ARA&A*, 28, 215
 Dopita, M., & Sutherland, R. 2010, *Astrophysics of the Diffuse Universe*, Astronomy and Astrophysics Library (Springer)
 Draine, B. T. 2011, *Physics of the Interstellar and Intergalactic Medium*, ed. D. N. Spergel (Princeton University Press)
 Einasto, J. 1965, *Trudy Astrofizicheskogo Instituta Alma-Ata*, 5, 87
 Fox, A. J., Richter, P., Wakker, B. P., et al. 2013, *ApJ*, 772, 110
 Fox, A. J., Wakker, B. P., Barger, K. A., et al. 2014, *ApJ*, 787, 147
 Fox, A. J., Bordoloi, R., Savage, B. D., et al. 2015, *ApJ*, 799, L7
 Fujimoto, M., & Sofue, Y. 1976, *A&A*, 47, 263
 Gao, L., Navarro, J. F., Cole, S., et al. 2008, *MNRAS*, 387, 536
 Gatto, A., Fraternali, F., Read, J. I., et al. 2013, *MNRAS*, 433, 2749
 Graczyk, D., Pietrzyński, G., Thompson, I. B., et al. 2014, *ApJ*, 780, 59
 Greivich, J., & Putman, M. E. 2009, *ApJ*, 696, 385
 Gunn, J. E., & Gott, III, J. R. 1972, *ApJ*, 176, 1
 Guo, F., & Mathews, W. G. 2012, *ApJ*, 756, 181
 Haffner, L. M., Reynolds, R. J., Tufte, S. L., et al. 2003, *ApJS*, 149, 405
 Henley, D. B., Shelton, R. L., Kwak, K., Joung, M. R., & Mac Low, M.-M. 2010, *ApJ*, 723, 935
 Ibata, R. A., Gilmore, G., & Irwin, M. J. 1994, *Nature*, 370, 194
 Jeans, J. H. 1915, *MNRAS*, 76, 70
 Jin, S., & Lynden-Bell, D. 2008, *MNRAS*, 383, 1686
 Kafle, P. R., Sharma, S., Lewis, G. F., & Bland-Hawthorn, J. 2014, *ApJ*, 794, 59
 Kalberla, P. M. W., Burton, W. B., Hartmann, D., et al. 2005, *A&A*, 440, 775
 Kallivayalil, N., van der Marel, R. P., & Alcock, C. 2006a, *ApJ*, 652, 1213
 Kallivayalil, N., van der Marel, R. P., Alcock, C., et al. 2006b, *ApJ*, 638, 772
 King, I. R. 1966, *AJ*, 71, 64
 Kramida, A., Ralchenko, Y., Reader, J., & NIST ASD Team. 2014, *NIST Atomic Spectra Database (ver. 5.2)*, NIST Atomic Spectra Database (ver. 5.2), [Online]. Available: <http://physics.nist.gov/asd> [2015, February 16]. National Institute of Standards and Technology, Gaithersburg, MD.
 Kuzmin, G. G. 1956, *Astr. Zh.*, 33
 Lehner, N., & Howk, J. C. 2011, *Science*, 334, 955
 Lehner, N., Howk, J. C., Thom, C., et al. 2012, *MNRAS*, 424, 2896
 Liska, R., & Wendroff, B. 2003, *SIAM Journal on Scientific Computing*, 25, 995
 Lockman, F. J., Benjamin, R. A., Heroux, A. J., & Langston, G. I. 2008, *ApJ*, 679, L21
 Madsen, G. J. 2012, in *EAS Publications Series*, Vol. 56, EAS Publications Series, ed. M. A. de Aveliz, 281–284
 Martin, P. G. 1988, *ApJS*, 66, 125
 Mastropietro, C., Moore, B., Mayer, L., Wadsley, J., & Stadel, J. 2005, *MNRAS*, 363, 509
 Mathewson, D. S., Cleary, M. N., & Murray, J. D. 1974, *ApJ*, 190, 291
 McClure-Griffiths, N. M., Madsen, G. J., Gaensler, B. M., McConnell, D., & Schnitzeler, D. H. F. M. 2010, *ApJ*, 725, 275
 Meurer, G. R., Bicknell, G. V., & Gingold, R. A. 1985, *Proceedings of the Astronomical Society of Australia*, 6, 195
 Michie, R. W., & Bodenheimer, P. H. 1963, *MNRAS*, 126, 269
 Miller, M. J., & Bregman, J. N. 2013, *ApJ*, 770, 118
 —. 2015, *ApJ*, 800, 14
 Miyamoto, M., & Nagai, R. 1975, *PASJ*, 27, 533
 Mohr, P. J., Taylor, B. N., & Newell, D. B. 2012, *Rev. Mod. Phys.*, 84, 1527
 Navarro, J. F., Frenk, C. S., & White, S. D. M. 1996, *ApJ*, 462, 563
 Nichols, M., & Bland-Hawthorn, J. 2009, *ApJ*, 707, 1642
 Nichols, M., Mirabal, N., Agertz, O., Lockman, F. J., & Bland-Hawthorn, J. 2014, *MNRAS*, 442, 2883
 Nidever, D. L., Majewski, S. R., & Burton, W. B. 2008, *ApJ*, 679, 432
 Nidever, D. L., Majewski, S. R., Butler Burton, W., & Nigra, L. 2010, *ApJ*, 723, 1618
 Nuza, S. E., Parisi, F., Scannapieco, C., et al. 2014, *MNRAS*, 441, 2593
 Omidvar, K. 1983, *Atomic Data and Nuclear Data Tables*, 28, 1
 Oort, J. H. 1970, *A&A*, 7, 381
 Pequignot, D., Petitjean, P., & Boisson, C. 1991, *A&A*, 251, 680
 Planck Collaboration, Ade, P. A. R., Aghanim, N., et al. 2014, *A&A*, 571, A16
 Plummer, H. C. 1911, *MNRAS*, 71, 460
 Portail, M., Wegg, C., Gerhard, O., & Martínez-Valpuesta, I. 2015, *MNRAS*, 448, 713
 Press, W. H., Teukolsky, S. A., Vetterling, W. T., & Flannery, B. P. 1992, *Numerical Recipes in C*, 2nd edn. (Cambridge University Press)
 Putman, M. E., Bland-Hawthorn, J., Veilleux, S., et al. 2003, *ApJ*, 597, 948
 Putman, M. E., Gibson, B. K., Staveley-Smith, L., et al. 1998, *Nature*, 394, 752
 Putman, M. E., Thom, C., Gibson, B. K., & Staveley-Smith, L. 2004, *ApJ*, 603, L77
 Retana-Montenegro, E., van Hese, E., Gentile, G., Baes, M., & Frutos-Alfaro, F. 2012, *A&A*, 540, A70
 Reynolds, R. J., Tufte, S. L., Haffner, L. M., Jaehnig, K., & Percival, J. W. 1998, *PASA*, 15, 14
 Richter, P., Fox, A. J., Wakker, B. P., et al. 2013, *ApJ*, 772, 111
 Shull, J. M., Roberts, D., Giroux, M. L., Penton, S. V., & Fardal, M. A. 1999, *AJ*, 118, 1450
 Snowden, S. L., Freyberg, M. J., Kuntz, K. D., & Sanders, W. T. 2000, *ApJS*, 128, 171
 Spitzer, Jr., L. 1956, *ApJ*, 124, 20
 Sternberg, A., McKee, C. F., & Wolfire, M. G. 2002, *ApJS*, 143, 419
 Storey, P. J., & Hummer, D. G. 1995, *MNRAS*, 272, 41
 Su, M., Slatyer, T. R., & Finkbeiner, D. P. 2010, *ApJ*, 724, 1044
 Sutherland, R. S. 2010, *Ap&SS*, 327, 173
 Sutherland, R. S., & Bicknell, G. V. 2007, *ApJS*, 173, 37
 Suto, Y., Sasaki, S., & Makino, N. 1998, *ApJ*, 509, 544
 Tufte, S. L. 1997, PhD thesis, THE UNIVERSITY OF WISCONSIN - MADISON
 Wakker, B. P. 2001, *ApJS*, 136, 463
 Walker, A. R. 2012, *Ap&SS*, 341, 43
 Wannier, P., & Wrixon, G. T. 1972, *ApJ*, 173, L119
 Weiner, B. J., Vogel, S. N., & Williams, T. B. 2002, in *Astronomical Society of the Pacific Conference Series*, Vol. 254, Extragalactic Gas at Low Redshift, ed. J. S. Mulchaey & J. T. Stocke, 256
 Weiner, B. J., & Williams, T. B. 1996, *AJ*, 111, 1156
 Weymann, R. J., Vogel, S. N., Veilleux, S., & Epps, H. W. 2001, *ApJ*, 561, 559
 Yao, Y., & Wang, Q. D. 2007, *ApJ*, 658, 1088

premise justifying this approach is the relative low masses of the bulge ($\sim 10^{-2}$) and the disc ($\sim 10^{-1}$) with respect to the mass of the DM halo, and the limited range over which their respective contribution may be important. Our reader will

APPENDIX

THE GAS DENSITY PROFILE IN THE PRESENCE OF A MASSIVE DISC

We ignored in our model potential the contribution of other components of the Galaxy, notably the disc and the bulge. Our

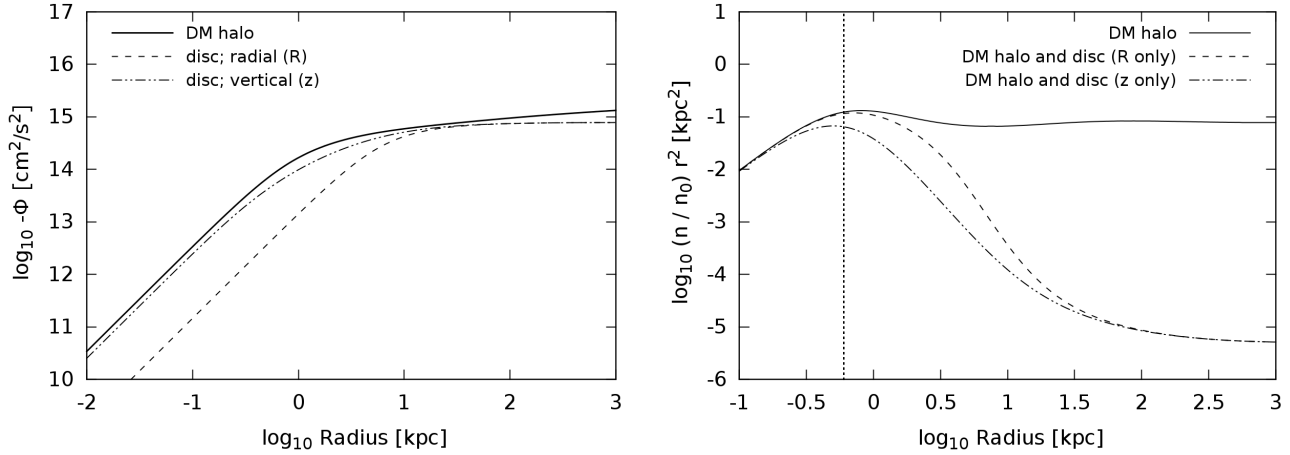


FIG. 9.— Left: Potential of an isothermal DM halo only, and including the potential of a Miyamoto & Nagai (1975) disc in radial (R) and vertical (z) direction (equation A1). Right: Normalized density profile of gas in hydrostatic equilibrium with the gravitational potential as given by equation A2, adopting $\tau = 1$. The vertical dotted line indicates distance from the potential centre corresponding to the core radius. Note that each density profile has been scaled by r^2 . At distances $r \gg r_c$ from the potential centre, the density is flat in this scaling, indicating that it behaves as $\rho(r) \propto r^{-2}$ (equation 13 adopting $\tau = 1$), regardless of the presence of a disc.

hopefully agree that we do not perpetrate a too serious fault because of neglecting the contribution of the bulge. We now explain in more detail the implications of our neglecting the contribution of the disc.

Perhaps the most realistic description of the Galactic disc potential is the Miyamoto & Nagai (1975, henceforth MN) model given by

$$\Phi_{\text{MN}}(R, z) = -\frac{GM_{\text{disc}}}{[R^2 + (a + w)^2]^{1/2}}. \quad (\text{A1})$$

with $w^2 \equiv z^2 + b^2$, with R and z the cylindrical coordinates, and where a and b are the scale length and scale height, respectively, and M_{disc} is the total mass of the disc. The MN model includes as limiting cases the Plummer (1911) and Kuzmin (1956) models, respectively, when $a \rightarrow 0$ and $b \rightarrow 0$. Both these models rely on assumptions closely related to the assumptions behind the isothermal sphere, and therefore their respective potentials behave similarly near the centre (Figure 9, left). Given the masses of the Galactic DM halo and disc, and the scale parameters we derived here, it turns out that the isothermal DM halo dominates the potential at all scales, although the contribution from the disc is comparable at $r \lesssim 10$ kpc.

Far away from the centre, i.e. for large values of R and/or z , the MN potential approaches that of a point mass $\Phi(r) \propto -r^{-1}$, where $r^2 = R^2 + z^2$. The function r^{-1} grows less rapidly than $\log r$ away from $r = 0$, and therefore at large radii the behavior of the density in hydrostatic equilibrium with a composite (i.e. DM halo plus disc) potential will be dominated by the potential of the DM halo. This is illustrated in the right panel of Figure 9, which shows the (normalized) density profile of gas in hydrostatic equilibrium with the potential of an isothermal DM-halo, and with a composite potential consisting of the potential of a DM halo and a MN disc. Note that the density profile is weighted by r^2 such that the nr^2 is constant where $n \propto r^2$. Clearly, while the density of gas in a DM only Galactic potential falls off as r^2 already at $r < 10$ kpc, the contribution of a disc steepens the density fall-off with radius, only to recover at $r \gtrsim 50$ kpc.

Thus, the presence of a MN disc merely rescales the density profile (at $r \gg r_c$), as far as the density far away from the

centre is concerned, and this rescaling can be absorbed when normalizing the density to the adopted (observed) value at a given radius.

Let us finally note that any arbitrary number of components, say $\sum_i \Phi'(r)$, may be added to the potential of the isothermal DM halo, and the resulting gas density profile simply obtained from

$$n(r) = n_0 \exp \left\{ \tau \left[W(r/r_c) + \frac{1}{\sigma^2} \sum_i \Phi'(r) \right] \right\}. \quad (\text{A2})$$

POTENTIAL-DENSITY PAIRS

The general strategy to find the potential corresponding to a given density profile (Sternberg et al. 2002; Nichols & Bland-Hawthorn 2009) consists in solving the spherically symmetric Poisson equation¹⁰

$$\frac{1}{r^2} \frac{d}{dr} \left(r^2 \frac{d\Phi}{dr} \right) = -4\pi G \rho(r)$$

in two steps.

First, define a scale-free *density function* $f_\rho(x)$ via

$$\rho(r) = \rho_c f_\rho(x),$$

where ρ_c is the core (or scale) density. For instance, the density function corresponding to a NFW and an Einasto profile are given by

$$f_\rho^{\text{NFW}}(x) = [x(1+x)^2]^{-1}, \quad (\text{B1})$$

and

$$f_\rho^{\text{EIN}}(x) = \exp \left\{ -\frac{2}{\alpha} [x^\alpha - 1] \right\}, \quad (\text{B2})$$

respectively (cf. equations 5 and 6). Use the density function thus obtained to compute the mass enclosed within a given radius r ,

$$M(r) = 4\pi \int_0^r \rho(y) y^2 dy = 4\pi \rho_c r_c^3 \int_0^x f_\rho(y) y^2 dy \equiv M_c f_M(x),$$

¹⁰ We include an explicit minus sign on the right-hand-side such that $\Phi(r) \leq \Phi_0$ for $r \geq 0$, where Φ_0 is the zero-point.

where the spherical *mass function*

$$f_M(x) \equiv 4\pi \int_0^x f_\rho(y) y^2 dy, \quad (\text{B3})$$

and the *core mass*

$$M_c \equiv \rho_c r_c^3 \quad (\text{B4})$$

have been defined.

Second, integrate the mass function to obtain a *potential function*

$$f_\Phi(x) \equiv \int_x^\infty f_M(y) y^{-2} dy. \quad (\text{B5})$$

The physical mass and the physical potential are recovered, respectively, using

$$M(r) = M_c f_M(r/r_c), \quad (\text{B6})$$

and

$$\Phi(r) = -v_s^2 f_\Phi(r/r_c), \quad (\text{B7})$$

where v_s is the *scale velocity*.

Given that two integrations are involved in this procedure, only two of the constants r_c , ρ_c , M_c , and v_s are independent, and the following relation holds:

$$v_s^2 = \frac{GM_c}{r_c} = G \rho_c r_c^2. \quad (\text{B8})$$

Thus, a particular (spherically symmetric) DM halo may be completely specified by its corresponding density profile and two scale parameters, for example, r_s and v_s .

In order to define our isothermal DM halo, and to compare its properties to other commonly adopted models, we numerically integrate the system of ODE (equations 1 and 2) to obtain the scale-free potential, the scale free density, and the scale-free mass (equation B3) of the isothermal DM halo. Also, we integrate the density function of both a NFW profile (equation B1) and an Einasto profile (equation B2) to obtain the corresponding scale-free mass and the corresponding scale free potential (B5). We perform the numerical integration¹¹ in each case over the range $x \in [10^{-4}, 10^4]$, to an absolute precision of $\delta x \leq 10^{-8}$.

H α RECOMBINATION COEFFICIENT

We briefly present here a full derivation of the recombination coefficient determining the H α emission by ionized gas, $\alpha_B^{(\text{H}\alpha)}$, as well as a description of the approach we follow to calculate $\alpha_B^{(\text{H}\alpha)}$ at different temperatures.

The emission of H α photons (in a parcel of gas) is governed by the ionization state of the gas, effectively determined by the electron density n_e , but most importantly by the H II recombination channels. The emission of H α photons corresponds to the electronic transition $n = 3 \rightarrow 2$, and the recombination of H II to the level $n = 1$ is irrelevant if the gas is optically thick to ionizing photons (case B recombination; Baker & Menzel 1938, see also Dopita & Sutherland 2010). However, not every electron that recombines to the $n = 2$ level will emit an H α photon, since there is more than one channel leading to this level at recombination.

In general, in order to calculate the number of photons emitted through the transition from a state defined by the quantum

¹¹ We use for this purpose the routine `odeint` provided by the *Numerical Recipes* (Press et al. 1992), modified to perform calculations with double precision (64 bytes).

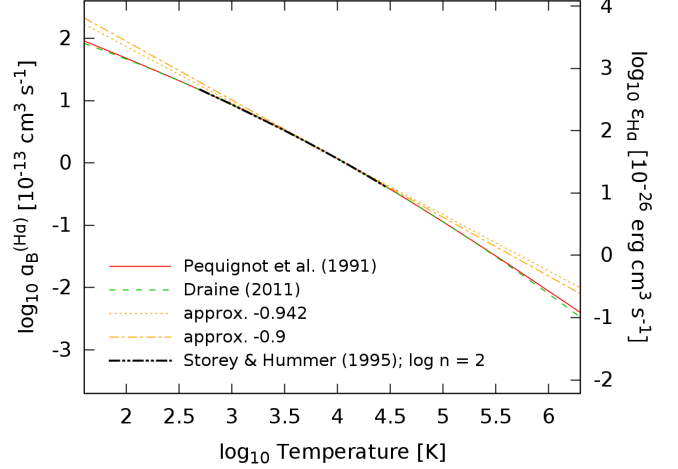


FIG. 10.— H α recombination coefficient as a function of electron temperature given by the fitting formulae (C2; red) and (C3; green). The orange curves show the approximation to (C3) obtained by ignoring the logarithmic term in the exponent, or even by replacing the index of the power law by -0.9 (rather than $-0.942 - 0.031 \ln[T/10^4 \text{ K}]$), respectively. The alternative y -axis on the right indicates the corresponding H α volume emission rate $\epsilon_{\text{H}\alpha}$ (equation D1). The black curve indicates the H α volume emission rate given by Storey & Hummer (1995).

numbers $n'l'$ to a new (energetically lower) state nl after recombination, it is necessary to know: 1) the population of state $n'l'$ either through direct recombination to that level or through recombination to a higher level and subsequent cascading, also known as *effective recombination coefficient* $\alpha_{n'l'}^{(c)}$; and 2) the probability, or *branching ratio*, $P(n'l' \rightarrow nl)$ that the atom decays through emission of a photon from level $n'l'$ to level nl (see e.g., Martin 1988). Thus,

$$\alpha_{n \rightarrow n}^{\text{eff}} = \sum_{l', l} \alpha_{n'l'}^{(c)} P(n'l' \rightarrow nl).$$

gives the effective *radiation* recombination coefficient from state n' (taking into account all of its sub-levels l' to the state n and all its sub-levels l . In the case of $n' = 3$ ($l' = s, p, d$) and $n = 2$ ($l = s, p$), the above expression gives the H α recombination coefficient.¹²

Branching ratios for hydrogen-like atoms have been calculated and tabulated by, e.g., Omidvar (1983). And effective recombination coefficients $\alpha_{n'l'}^{(c)}$ for both Case A and B have been tabulated on a grid of electron densities n_e and electron temperatures T_e by different authors (e.g. Martin 1988; Storey & Hummer 1995).

Using the branching ratios from Omidvar (1983, their Tables III B / C), and the effective recombination coefficients from Storey & Hummer (1995) for $n_e = 10^2 \text{ cm}^{-3}$ (the lowest density they consider; see their Section 4, data file `r1b0100.d`, entry 'R_NU = 3'), we find that the effective radiation coefficient for the (H I) H α transition after recombination for Case

¹² Note that the (allowed) transitions $n = 3 \rightarrow 2$ have very similar energies and can thus be considered as a single transition for practical (i.e., astrophysical) purposes.

B at $T_e = 10^4$ K is¹³

$$\begin{aligned}
\alpha_B^{(\text{H}\alpha)} &\equiv \alpha_{B,3\rightarrow 2}^{\text{eff}}(n_e = 10^2 \text{ cm}^{-3}; T_e = 10^4 \text{ K}) \\
&= \sum_{l'=s,p,d} \sum_{l=s,p} \alpha_{3l'}^{(c)} P(3l' \rightarrow 2l) \\
&= \alpha_{3s}^{(c)} [P(3s \rightarrow 2s) + P(3s \rightarrow 2p)] \\
&\quad + \alpha_{3p}^{(c)} [P(3p \rightarrow 2s) + P(3p \rightarrow 2p)] \\
&\quad + \alpha_{3d}^{(c)} [P(3d \rightarrow 2s) + P(3d \rightarrow 2p)] \\
&= (1.534 \times 10^{-4} \text{ cm}^3 \text{ s}^{-1}) [0.000 + 1.00] \\
&\quad + (3.726 \times 10^{-4} \text{ cm}^3 \text{ s}^{-1}) [1.00 + 0.000] \\
&\quad + (6.426 \times 10^{-4} \text{ cm}^3 \text{ s}^{-1}) [0.000 + 1.00] \\
&\approx 1.169 \times 10^{-13} \text{ cm}^3 \text{ s}^{-1}. \tag{C1}
\end{aligned}$$

For comparison, the *total* case B recombination coefficient at $T = 10^4$ K is $\alpha_B = 2.585 \times 10^{-13} \text{ cm}^3 \text{ s}^{-1}$ (Storey & Hummer 1995, their Table 1). Hence, only about half of the time does an electron that recombines to the level $n = 2$ of an hydrogen atom emits an H α photon.

Now, in order to describe the temperature dependence of $\alpha_B^{(\text{H}\alpha)}$, we adopt the fitting formula by Pequignot et al. (1991, their Equation 1 and parameter values from Table 2)

$$\alpha(T) = 10^{-13} \text{ cm}^3 \text{ s}^{-1} z \frac{a (T/10^4 \text{ K})^b}{1 + c (T/10^4 \text{ K})^d},$$

which is accurate to two percent in the range $40 \text{ K} < T < 2 \times 10^4 \text{ K}$. The values of the fitting parameters appropriate for the effective Case B recombination coefficient for hydrogen and for the transition $n = 3 \rightarrow 2$ are $z = 1$, $a = 2.708$, $b = -0.648$, $c = 1.315$, and $d = 0.523$. For convenience, we recast the above equation as

$$\begin{aligned}
\alpha_B^{(\text{H}\alpha)}(T) &= (1.169 \times 10^{-13} \text{ cm}^3 \text{ s}^{-1}) \\
&\quad \times \frac{(1 + c)(T/10^4 \text{ K})^b}{1 + c (T/10^4 \text{ K})^d}. \tag{C2}
\end{aligned}$$

An alternative fitting formula is given by Draine (2011, their Equation 14.8), which in our notation reads

$$\begin{aligned}
\alpha_B^{(\text{H}\alpha)}(T) &= (1.169 \times 10^{-13} \text{ cm}^3 \text{ s}^{-1}) \\
&\quad \times (T/10^4 \text{ K})^{-0.942 - 0.031 \ln(T/10^4 \text{ K})}, \tag{C3}
\end{aligned}$$

which is accurate to two percent in the range $10^3 \text{ K} < T < 3 \times 10^4 \text{ K}$. We compare both these results in Figure 10. It is not uncommon to find in the literature an approximation to the (already an approximation) fit given by equation (C3) obtained by ignoring the logarithmic term in the exponent, or even by replacing the index of the power law by -0.9 (rather than $-0.942 - 0.031 \ln(T/10^4 \text{ K})$). As shown in Figure 10, *these* approximations are only valid for a narrow range of temperatures around $T = 10^4 \text{ K}$.

We give, for completeness, the temperature dependence of the total case B recombination coefficient (Pequignot et al.

1991)

$$\begin{aligned}
\alpha_B(T) &= (2.585 \times 10^{-13} \text{ cm}^3 \text{ s}^{-1}) \\
&\quad \times \frac{(1 + c')(T/10^4 \text{ K})^{b'}}{1 + c' (T/10^4 \text{ K})^{d'}}. \tag{C4}
\end{aligned}$$

with $b' = -0.6166$, $c' = 0.6703$, and $d' = 0.5300$.

H α - AND H I 21 CM EMISSION

In the following sections we describe our approach to compute the H α and H I 21 cm emission spectra, and the corresponding H α surface brightness from our simulations.

H α surface brightness

In order to calculate the observed H α gas emission at each cell in our simulation volume we proceed as follows. We define the H α *volume emission rate* (in $\text{erg cm}^3 \text{ s}^{-1}$) through

$$\epsilon_{\text{H}\alpha}(T) = E_{\text{H}\alpha} \alpha_B^{(\text{H}\alpha)}(T), \tag{D1}$$

where $E_{\text{H}\alpha} \equiv h\nu_{\text{H}\alpha} = hc/\lambda_{\text{H}\alpha} = 3.03 \times 10^{-12} \text{ erg}$ is the energy per H α photon.¹⁴ The corresponding luminosity density, i.e. power per unit volume, is

$$l_{\text{H}\alpha}(n, T) = n_{\text{HII}} n_e \epsilon_{\text{H}\alpha}(T), \tag{D2}$$

where n_e and n_{HII} are the electron number density and the H II number density, respectively, and the argument n is a generic dependence on density.¹⁵ The H α luminosity (in erg s^{-1}) of a source with a volume δV is simply

$$\delta L_{\text{H}\alpha}(n, T) = l_{\text{H}\alpha}(n, T) \delta V,$$

and the corresponding total intensity (or irradiance; in $\text{erg s}^{-1} \text{ cm}^{-2}$) through the area δA enclosing the cell volume δV is

$$I_{\text{H}\alpha}(n, T) = \frac{\delta L_{\text{H}\alpha}(n, T)}{\delta A} = l_{\text{H}\alpha}(n, T) \frac{\delta V}{\delta A}.$$

Finally, the specific intensity or *surface brightness*¹⁶ (in $\text{erg s}^{-1} \text{ cm}^{-2} \text{ sr}^{-1}$) is obtained by considering that the intensity is spread uniformly over the entire celestial sphere which subtends a total solid angle of $4\pi \text{ sr}$,

$$\mu_{\text{H}\alpha} = \frac{1}{4\pi} I_{\text{H}\alpha}(n, T).$$

The total area and volume of one cell in our simulations are $\delta A = 6 (\delta x)^2$ and $\delta V = (\delta x)^3$, respectively. Hence, the H α surface brightness of one cell

$$\mu_{\text{H}\alpha} = \frac{1}{24\pi} l_{\text{H}\alpha}(n, T) \delta x, \tag{D3}$$

which is independent of the adopted distance, as it should.

Now, adopting a hydrogen, helium, and heavy-element mass fractions¹⁷ $X = 0.7154$ and $Y = 0.2703$, respectively (solar

¹⁴ We use the Ritz (air) wavelength of the Balmer H α transition, $\lambda_{\text{H}\alpha} = 6562.81 \text{ \AA}$ (Kramida et al. 2014), which corresponds to a frequency $\nu_{\text{H}\alpha} = 4.568 \times 10^{14} \text{ s}^{-1}$.

¹⁵ Strictly speaking, $\alpha_B^{(\text{H}\alpha)}$ and thus $\epsilon_{\text{H}\alpha}$ also depend on n . But here we are using the value of the recombination coefficient tabulated for the lowest density available, $n_e = 10^2 \text{ cm}^{-3}$ (see above).

¹⁶ Actually, *radiance*. Strictly speaking, surface brightness has the units of magnitude (i.e., logarithmic luminosity) per square arcsecond.

¹⁷ For our adopted metallicity of 10 percent the (bulk) solar value ($Z = 0.0142$; Asplund et al. 2009), the contribution of heavy elements to the electron density can be neglected.

¹³ Note that Omidvar (1983, their Table III B) gives $P(3p \rightarrow 2s) \equiv \beta_T(2s, 3p) = 0.118$. The complementary probability is the fraction of transitions to the $1s$ state, i.e., $P(3p \rightarrow 1s) = 0.882$. However, since we are considering recombination Case B, $P(3p \rightarrow 1s) \equiv 0$ by definition and consequently $P(3p \rightarrow 2s) \equiv 1$.

bulk composition given by Asplund et al. 2009), and assuming the gas is fully ionized¹⁸, the electron density is linked to the hydrogen density by

$$n_e = n_H + n_{He} = [1 + (Y/4X)] n_H \approx 1.09 n_H. \quad (D4)$$

Moreover, $n_H \approx n_{HII}$, and thus $n_e \approx 1.09 n_{HII}$, which is the approximation we use in our models.

The quantity given by equation (D3) is the actual observable, and it is conventionally given in the research field of diffuse emission in units of $\text{erg s}^{-1} \text{cm}^{-2} \text{arcsec}^{-2}$, which can be obtained by simply dividing the above expression by the conversion factor between sr and arcsec^2 , $f_{\text{sr} \rightarrow \text{arc}^2} \equiv (180 \times 3600/\pi)^2 \text{arcsec}^2 \text{sr}^{-1}$. The final expression thus reads, plugging in all relevant quantities, and expressing electron densities in terms of H II densities as explained above,

$$\mu_{H\alpha} = 1.09 K_\epsilon (n_{HII}^2 \delta x) \alpha_B^{(H\alpha)}(T),$$

where we have grouped all constant factors other than 1.09 into

$$K_\epsilon \equiv \frac{E_{H\alpha}}{24\pi f_{\text{sr} \rightarrow \text{arc}^2}} = 9.44 \times 10^{-25} \text{erg arcsec}^{-2}.$$

Alternatively, surface brightness can be expressed in units of Rayleigh, which is a measure of *photon* radiance, such that 1 Rayleigh (R) corresponds to $10^6/4\pi \text{photons cm}^{-2} \text{s}^{-1} \text{sr}^{-1}$ (Baker & Romick 1976). Thus, 1 Rayleigh of H α photons corresponds to $R_{H\alpha}(T) \equiv R \times E_{H\alpha} = 2.41 \times 10^{-7} \text{erg cm}^{-2} \text{s}^{-1} \text{sr}^{-1} \text{R}^{-1}$. If expressed in units of arcsec^{-2} (rather than sr^{-1}), then the value is¹⁹ $R_{H\alpha}(T) = 5.66 \times 10^{-18} \text{erg cm}^{-2} \text{s}^{-1} \text{arcsec}^{-2} \text{R}^{-1}$. Thus, if required in units of Rayleigh, one then simply uses

$$\mu_{H\alpha} = 1.09 K_R (n_{HII}^2 \delta x) \alpha_B^{(H\alpha)}(T),$$

where

$$K_R \equiv \frac{K_\epsilon}{R_{H\alpha}} \approx 1.67 \times 10^{-7} \text{cm}^2 \text{s R}.$$

It is also common to adopt an equivalence between the H α surface brightness, $\mu_{H\alpha}$, and the corresponding *emission measure*,

$$\mathcal{E}_m \equiv \int n_e^2 ds,$$

which is essentially an integral of recombinations along the sightline. The derivation of this equivalence follows directly from the definition of the surface brightness, the relationship between n_e and n_{HII} (see equation D4), and the use of the appropriate units:

$$\begin{aligned} \mu_{H\alpha} &= \frac{1}{4\pi} (n_e n_{HII}) (1 \text{ pc}) \alpha_B^{(H\alpha)} \\ &= \frac{10^3}{4\pi} \frac{n_e^2 (1 \text{ pc})}{1.09 \times 10^3} \alpha_B^{(H\alpha)} \\ &= \frac{10^3}{4\pi} \frac{3.08 \times 10^{18} \text{cm}^{-5}}{1.09 \times 10^3} (1.169 \times 10^{-13} \text{cm}^3 \text{s}^{-1}) \\ &\approx 3.30 \times 10^2 \text{mR} \end{aligned}$$

Thus, an emission measure of $1 \text{cm}^{-6} \text{pc} \hat{=} 330 \text{mR}$ (at 10^4K).

¹⁸ We assume that helium is only singly ionized, given that the ionization energy of He 2 is comparatively high ($E \approx 54.4 \text{eV}$; Kramida et al. 2014).

¹⁹ $1 \text{sr} \hat{=} \left(\frac{180 \times 3600}{\pi}\right)^2 \text{arcsec}^2$.

H α - and H I line profiles

The monochromatic H α line emissivity at frequency ν of a parcel of ionized gas with density n and temperature T located at s is given by the H α luminosity density ($\text{erg cm}^{-3} \text{s}^{-1}$) at s per unit steradian per unit frequency (see equations D1 and D2),

$$j_{H\alpha}(\nu, s) = \frac{1}{24\pi} l_{H\alpha}(n, T) \phi(\nu), \quad (D5)$$

Note that n and T , and hence $l_{H\alpha}$, all depend on s . Also, we have included a factor 1/6 to account for fact that we are observing along a single ray (or face of a cubic cell; compare equation D3).

Assuming that the spread in frequency is dominated by the thermal motion of the atoms, and that the velocities of the atoms follow a Maxwell-Boltzmann distribution, the H α emission of a parcel of gas at temperature T located at s and measured at velocity v (with respect to the bulk motion of the gas) is given by

$$j_{H\alpha}(v, s) = \frac{1}{24\pi^{3/2}} \frac{1}{b_T} l_{H\alpha}(T, s) \phi(v). \quad (D6)$$

where $\phi(v) = \exp[-v^2/b_T^2]$, and $b_T = (2kT/m_u)^{1/2}$.

Given that a single cell in our simulation volume represents the smallest parcel of gas we are able to resolve, the emissivity does not change across the cell, and the H α *monochromatic* intensity at velocity v measured at a given point s along the sightline of the gas emission within a single cell is given by

$$\begin{aligned} I_{H\alpha}(v, \mathbf{n}) &\equiv \int_{s'}^{s|\mathbf{n}} j_{H\alpha}(v, s') ds' \\ &\equiv j_{H\alpha}(v, \mathbf{n}) \int_{\text{cell}} ds' \\ &= j_{H\alpha}(v, \mathbf{n}) \delta x, \end{aligned} \quad (D7)$$

where δx is the linear size of a cell, and $\mathbf{n} \equiv (i, j, k)$ are the central coordinates (i.e., indices) of the cell with respect to the simulation grid. Note that we have assumed that the gas is optically thin to H α , such that the absorption by the gas parcels between the cell with coordinates \mathbf{n} and the detector can be ignored. It follows by virtue of equations (D3) and (D6) that

$$I_{H\alpha}(v, \mathbf{n}) = \mu_{H\alpha}(\mathbf{n}) \phi_{\mathbf{n}}(v), \quad (D8)$$

where we have attached a subindex \mathbf{n} to $\mu_{H\alpha}$ and ϕ to emphasize their dependence on the physical conditions (n, T) of the cell.

The H α intensity observed at velocity v_m (in the rest-frame of the H I gas at $t_{\text{sim}} = 0$) of a parcel of gas at \mathbf{n} with bulk velocity $v_{\mathbf{n}}$ is

$$I_{H\alpha}([v_m - v_{\mathbf{n}}], \mathbf{n}) = \mu_{H\alpha}(\mathbf{n}) \phi_{\mathbf{n}}(v_m - v_{\mathbf{n}}). \quad (D9)$$

Clearly, if the line profile is normalized, i.e.,

$$\int_{-\infty}^{+\infty} \phi_{\mathbf{n}}(v) dv \equiv 1,$$

the H α surface brightness of the cell is simply obtained using

$$\mu_{H\alpha}(\mathbf{n}) = \int_{-\infty}^{+\infty} I_{H\alpha}([v_m - v_{\mathbf{n}}], \mathbf{n}) dv_m. \quad (D10)$$

A similar approach is followed for the H I 21 cm emission. In brief, we spread the H I column density of each cell $N_{\text{HI}}(\mathbf{n}) -$

which we use as a proxy for the H I 21 cm emission intensity – in velocity according to

$$I_{\text{H I}}([v_m - v_n], \mathbf{n}) \equiv N_{\text{H I}}(\mathbf{n}) \phi_n(v_m - v_n). \quad (\text{D11})$$

Photoionisation

We include in our model the contribution of the cosmic UV background (UVB) ionizing radiation, which leads to a low, but non-negligible level of H α emission along the Stream. The evolution of the hydrogen neutral and ionized fractions, $x_{\text{H I}} \equiv n_{\text{H I}}/n$ and $x_{\text{H II}} \equiv n_{\text{H II}}/n$, respectively, where $n \equiv n_{\text{H I}} + n_{\text{H II}}$, in gas which is optically thick to ionizing photons obeys

$$\frac{dx_{\text{H I}}}{dt} = x_{\text{H II}} n_e \alpha_B - x_{\text{H I}} \Gamma_{\text{H I}} \quad (\text{D12})$$

$$\frac{dx_{\text{H II}}}{dt} = -\frac{dx_{\text{H I}}}{dt} \quad (\text{D13})$$

where $\alpha_B \equiv \alpha_B(T)$ is the case B *total* H I recombination coefficient (in $\text{cm}^3 \text{s}^{-1}$), and

$$\Gamma_{\text{H I}} \equiv 4\pi \int_{\nu_{\text{LL}}}^{\infty} \frac{\sigma_{\text{H}}(\nu) J_\nu}{h\nu} d\nu \quad (\text{D14})$$

is the H I photoionisation rate in photons per atom per second. Here, J_ν is the angle-averaged specific intensity of the UVB; $\nu_{\text{LL}} \approx 3.29 \times 10^{15} \text{ Hz}$ is the minimum photon frequency required to ionize hydrogen; and $\sigma_{\text{H}}(\nu) \approx \sigma_0 (\nu/\nu_{\text{LL}})^3$ is the hydrogen ionization cross section with $\sigma_0 = 6.3 \times 10^{-18} \text{ cm}^2$.

In photoionisation *equilibrium*, $dx_{\text{H I}}/dt \equiv 0$, and thus

$$(n_e n_{\text{H II}}) \alpha_B = n_{\text{H I}} \Gamma_{\text{H I}}, \quad (\text{D15})$$

assuming that the gas is highly ionized ($n_{\text{H}} \approx n_{\text{H II}}$).

The H α emission induced by the metagalactic ionizing radiation field along the sightline is thus given by equation (17), where the fraction of recombinations that produce an H α photon is

$$f_{\text{H}\alpha}(T) \equiv \frac{\alpha_B^{(\text{H}\alpha)}(T)}{\alpha_B(T)} \approx 0.452 g(T), \quad (\text{D16})$$

Here, g is a monotonically decreasing function of temperature (see equations C4 and C2)

$$g(T) = \left(\frac{1+c}{1+c'} \right) \left[\frac{1+c'(T/10^4 \text{ K})^{d'}}{1+c(T/10^4 \text{ K})^d} \right] (T/10^4 \text{ K})^{b-b'}, \quad (\text{D17})$$

which satisfies $g(10^4 \text{ K}) \equiv 1$, and $g \in (0.6, 1.3)$ for $T \in [10^3, 10^6] \text{ K}$.

Note that $f_{\text{H}\alpha}$ (through T) and $n_{\text{H I}}$ both vary along the sightline. An estimate of the H α signal resulting from the ionization by the cosmic UVB of gas at can nevertheless be obtained assuming the gas temperature to be uniform along the sightline. In this case, and inserting the appropriate numerical values we get

$$\mu_{\text{H}\alpha}^{(\text{phot})} \approx 452 \text{ mR} \left(\frac{N_{\text{H I}}}{10^{18} \text{ cm}^{-2}} \right) \left(\frac{\Gamma_{\text{H I}}}{10^{-12} \text{ s}^{-1}} \right), \quad (\text{D18})$$

where $N_{\text{H I}}$ is the integral of $n_{\text{H I}}$ along the sightline. Hence, for an H I ionization rate $\Gamma_{\text{H I}} \sim 10^{-13} \text{ s}^{-1}$ at $z = 0$ (upper limit; Weymann et al. 2001; Adams et al. 2011) and gas at 10^4 K with $N_{\text{H I}} \sim 10^{17} \text{ cm}^{-2}$, the H α signal resulting from the ionization by the cosmic UVB of gas at 10^4 K is roughly 5 mR.

Since we are not performing proper radiative transfer calculations, we limit the depth (along the sightline) of the gas ionized by the UVB to a value L_{max} defined by the condition that the column recombination equals the incident ionizing photon flux Φ_i :

$$\alpha_B \int_0^{L_{\text{max}}} (n_e n_{\text{H II}}) ds \stackrel{!}{=} \Phi_i, \quad (\text{D19})$$

where the ionizing photon flux (in photons $\text{cm}^{-2} \text{s}^{-1}$) is given by equation (18), which results from the definition

$$\Phi_i \equiv \pi \int_{\nu_{\text{LL}}}^{\infty} \frac{J_\nu}{h\nu} d\nu,$$

the definition (D14), and the assumption that the spectrum $J_\nu \propto \nu^{-\gamma}$. The above condition implies that all the ionizing photons be absorbed within a depth L_{max} , assuming the gas has been exposed to the (uniform) UV radiation field long enough to reach ionization equilibrium (which is well justified in the case of the Stream; see Bland-Hawthorn et al. 2013, their Appendix). Note that this condition is equivalent to restricting the ionizing effect of the UVB to a column of gas $\sim 10^{17} \text{ cm}^{-2}$. Indeed, using equations (D15) and (18), the condition (D19) becomes

$$\int_0^{L_{\text{max}}} n_{\text{H I}} ds = \frac{2}{3} N_{\text{H I}}(\text{LL}).$$

where $N_{\text{H I}}(\text{LL}) \equiv \sigma_0^{-1} \approx 1.6 \times 10^{17} \text{ cm}^{-2}$.

DESTRUCTION TIME-SCALES

The physical parameter determining the evolution (and survival) of the gas as well as the production of the H α emission are the (drift) velocity of the gas, v_h , the adiabatic sound velocity of the halo gas, c_h , and thus the Mach number $M \equiv v_h/c_h$; the cloud-to-halo density ratio $\eta \equiv \rho_w/\rho_h$; and the cloud-to-halo pressure ratio $\xi \equiv P_w/P_h$.

The dynamic (or ram) pressure²⁰ is given by (up to a multiplicative factor of order unity) $P_{\text{dyn}} = \rho v^2$. A gas blob of density ρ_w moving at velocity v through a medium of density ρ_h experiences a shock which, once (ram) pressure equilibrium has been reached (i.e. $\xi \sim 1$), travels trough the blob at a velocity $v_s = \eta^{-1/2} v_h$. The shock will eventually destroy the gas blob in about the time it takes to travel trough it (Bland-Hawthorn et al. 2007). Assuming the gas blob has a characteristic linear size d_c , the destruction (or survival) time scale is

$$\tau_w \equiv \frac{d_w}{v_s} = \eta^{1/2} \left(\frac{d_w}{v_h} \right). \quad (\text{E1})$$

Note that this time scale is of the same order (and actually analogue) to the growth time of a Kelvin-Helmholtz instability with a characteristic size $\lambda \equiv d_w$ at the interface of two media of densities ρ_w and ρ_h which satisfy $\rho_w/\rho_h \gg 1$ (equation E3). Indeed, a perturbation (or mode) of size $\lambda = 2\pi/k$, at the interface between two media with densities ρ_w and ρ_h moving with velocity v with respect to each other will grow in a time-scale $\tau = 2\pi/\omega$ given by

$$\omega = k v \frac{(\rho_w \rho_h)^{1/2}}{\rho_w + \rho_h} \quad (\text{E2})$$

²⁰ Or drag force per unit area

Note that for $\rho_w \gg \rho_h$ the above expression simplifies to $\omega \approx \eta^{-1/2} k v$, and thus the characteristic time scale in this case is

$$\tau_{\text{KH}} = \eta^{1/2} \left(\frac{\lambda}{v} \right). \quad (\text{E3})$$

And similarly for the development of Rayleigh-Taylor instabilities. In this case, a perturbation (mode) of size $\lambda = 2\pi/k$, at the interface between two media with densities $\rho_h > \rho_w$, where medium 1 is accelerated into medium 2 with acceleration a will grow in a time-scale given by (this is an approximation valid only for small modes, i.e $k \gg 1$)

$$\omega^2 = k a \frac{\rho_w - \rho_h}{\rho_w + \rho_h} \quad (\text{E4})$$

If $\rho_w \gg \rho_h$ the above expression simplifies to $\omega^2 \approx k a$, resulting in a characteristic time scale

$$\tau_{\text{RT}} = \left(2\pi \frac{\lambda}{a} \right)^{1/2}. \quad (\text{E5})$$

COMPLEMENTARY FIGURES

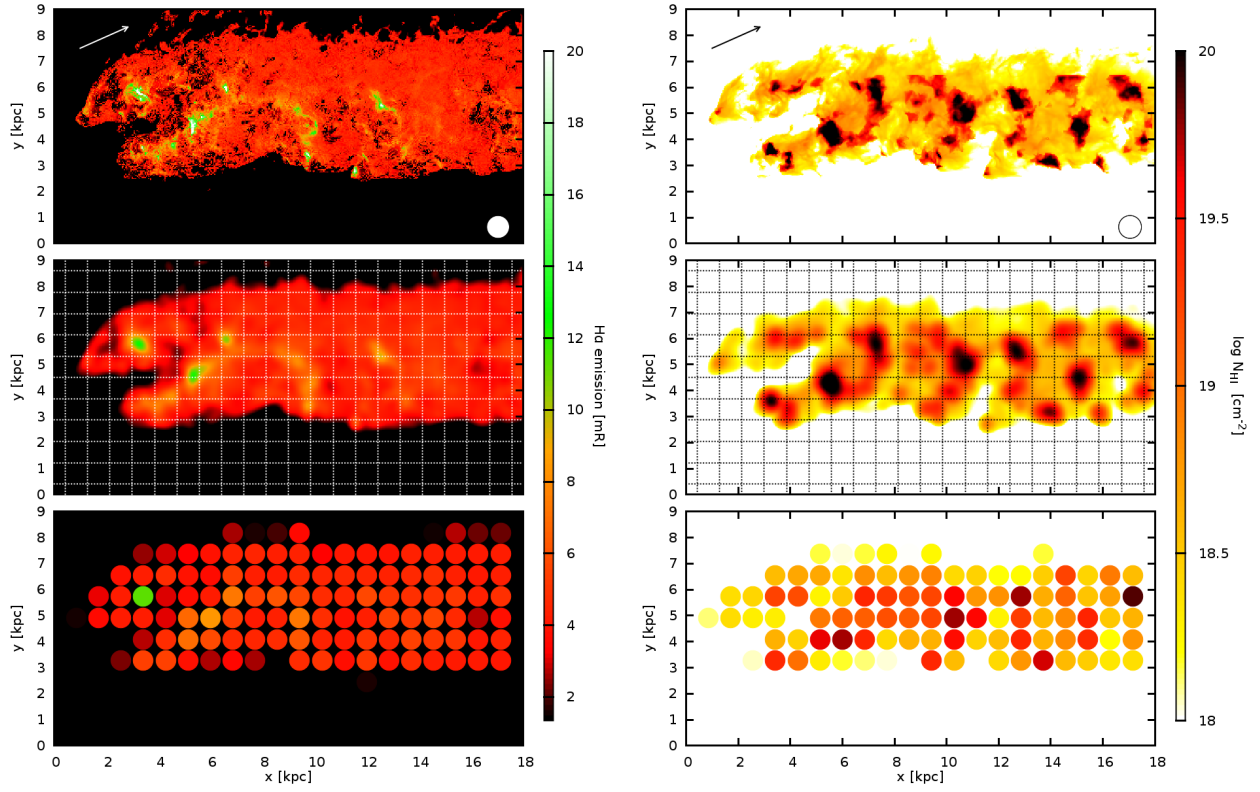


FIG. 11.— Similar to Figure 3 but projected along the z axis and for $t_{sim} = 120$ Myr.

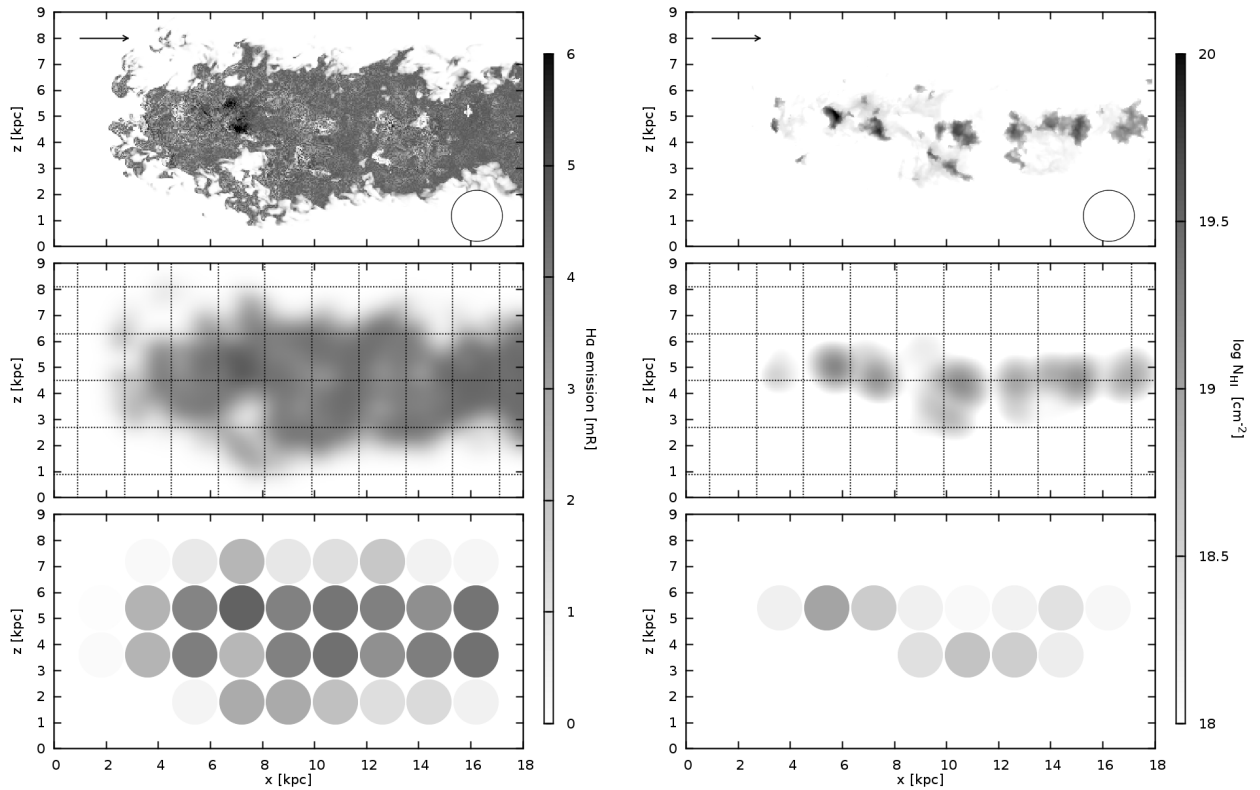


FIG. 12.— Similar to Figure 3 but assuming a Stream's distance over the SGP $r_{MS} = 125$ kpc. Note that the image is shown in the comoving frame of the model Stream.